NO Releasing and Anticancer Properties of Octahedral Ruthenium-Nitrosyl Complexes with Equatorial 1*H*-indazole Ligands

Evelina Orlowska,[†] Maria V. Babak,[‡] Orsolya Dömötör,[Δ] Eva A. Enyedy,[Δ] Peter Rapta,[ǁ] Michal Zalibera,[ǁ] Lukáš Bučinský,[ǁ] Michal Malček,[ǁ,○] Chinju Govind,[≠] Venugopal Karunakaran,[≠] Yusuf Chouthury Shaik Farid,[⌂] Tara McDonnell,[□] Dominique Luneau,[◊] Dominik Schaniel,[▽] Wee Han Ang, [‡] Vladimir B. Arion[†,*]

[†]Institute of Inorganic Chemistry, Faculty of Chemistry, University of Vienna, Währinger Strasse 42, A-1090 Vienna, Austria

[‡]Department of Chemistry, National University of Singapore, 3 Science Drive 2, 117543 Singapore

[Δ]Department of Inorganic and Analytical Chemistry, University of Szeged, Dom ter 7, H-6720 Szeged, Hungary

[ǁ]Slovak University of Technology, Institute of Physical Chemistry and Chemical Physics, Radlinského 9, SK-81237 Bratislava, Slovakia

[○]LAQV@REQUIMTE, Department of Chemistry and Biochemistry, Faculty of Sciences, University of Porto, Rua do Campo Alegre s/n, 4169-007 Porto, Portugal

[≠]Photosciences and Photonics section, Chemical Sciences and Technology Division, CSIR-National Institute for Interdisciplinary Science and Technology, Thiruvananthapuram 695019 Kerala, India

[⌂]School of Chemistry and Life Sciences, Nanyang Polytechnic, 180 Ang Moh Kio Ave 8, 569830, Singapore

[□]School of Biotechnology and Biomolecular Sciences, the University of New South Wales, Kensington, Sydney, NSW 2052, Australia

[◊]Laboratoire des Multimatériaux et Interfaces (UMR5615), Université Claude Bernard Lyon 1, Campus de la Doua, 69622 Villeurbanne, Cedex, France

[▽]Université de Lorraine, CNRS, CRM2, 54506 Nancy, France

*Corresponding author: E-mail: vladimir.arion@univie.ac.at

Abstract. With the aim of enhancing the biological activity of ruthenium-nitrosyl complexes, new complexes with four equatorially bound indazole ligands, namely *trans*-[RuCl(Hind)$_4$(NO)]Cl$_2$·H$_2$O (**[3]Cl$_2$·H$_2$O**) and *trans*-[RuOH(Hind)$_4$(NO)]Cl$_2$·H$_2$O (**[4]Cl$_2$·H$_2$O**) have been prepared from *trans*-[Ru(NO$_2$)$_2$(Hind)$_4$] (**[2]**). When the pH-dependent solution behavior of **[3]Cl$_2$·H$_2$O** and **[4]Cl$_2$·H$_2$O** was studied, two new complexes with deprotonated indazole ligands were isolated, namely [RuCl(ind)$_2$(Hind)$_2$(NO)] (**[5]**) and [RuOH(ind)$_2$(Hind)$_2$(NO)] (**[6]**). All prepared compounds were comprehensively characterized by spectroscopic (IR, UV–vis, ^{1}H NMR) techniques. Compound **[2]**, as well as **[3]Cl$_2$·2(CH$_3$)$_2$CO**, **[4]Cl$_2$·2(CH$_3$)$_2$CO** and **[5]·0.8CH$_2$Cl$_2$**, the latter three obtained by re-crystallization of the first isolated compounds (hydrates or anhydrous species) from acetone and dichlorometane, respectively, were studied by X-ray diffraction methods. The release of NO in complexes **[3]Cl$_2$** and **[4]Cl$_2$** triggered by one-electron reduction was investigated by cyclic voltammetry and resulting paramagnetic NO species were detected by EPR spectroscopy. The release of NO upon irradiation with blue light was investigated by IR, UV-vis and EPR spectroscopy and kinetics of NO release was discussed. The quantum yields of NO release were calculated and found to be low (3-6%), which could be explained by NO dissociation and recombination dynamics, assessed by femtosecond pump-probe spectroscopy. The geometry and electronic parameters of Ru species formed upon NO release were identified by DFT calculations. The complexes **[3]Cl$_2$** and **[4]Cl$_2$** showed considerable antiproliferative activity in human cancer cell lines with IC$_{50}$ values in low micromolar or submicromolar concentration range are suitable for further development as potential anticancer drugs. p53-dependence of Ru-NO complexes **[3]Cl$_2$** and **[4]Cl$_2$** was studied and p53-independent mode of action has been confirmed. The effects of NO release on the cytotoxicity of the complexes with or without light irradiation were investigated using NO scavenger carboxy-PTIO.

Introduction

Nitric oxide (NO) is known both as an air pollutant[1] as well as a physiological regulator[2] essential for neurotransmission, blood pressure control, antioxidant action and immunological responses.[3] In cells NO is mainly produced by conversion of L-arginine to L-citrulline in the presence of nitric oxide synthase (NOS). The down-regulation of NO synthesis in a variety of normal cells and in tumor cells is mediated by intracellular transforming growth factor-β1 (TGF-β1).[4] The control of cellular NO concentration, either by inhibiting its production or by targeted delivery can be achieved by using suitable metal complexes, and consequently, NO-scavenging and NO-releasing metal complexes are of great therapeutic interest.[5] NO as a ligand readily binds to transition metals, such as iron or ruthenium, forming stable M-NO adducts. Recently, it was reported that the anticancer effects of Ru(III)-based clinical lead candidates, KP1019/NKP1339 and NAMI-A, were at least in part due to their NO-scavenging properties, stemming from high affinity of ruthenium(III) to NO.[6,7] Scavenging of endogenous NO produced from NOS depletes its local concentration, thereby diminishing subsequent interactions with cellular targets.

Since the role of NO in tumor development can also be inhibitory, NO-donating compounds which release free NO hold great promises as anticancer agents. For example, high NO levels (>500 nM) induce apoptosis as a result of p53 activation and therefore, the exogenous delivery of cytotoxic levels of NO by NO-releasing drugs might be beneficial for the induction of apoptosis via p53 pathway.[8] Some NO-releasing compounds display spontaneous release of NO, while other compounds require external stimuli, such as enzymatic, photo-, thermal activation or redox events.[9] Ruthenium-nitrosyl complexes are excellent candidates for the delivery of exogenous NO, since the efficacy of NO release can be fine-tuned by modifying the structure of Ru complexes. Ruthenium exists in several oxidation states, whereas NO acts as a non-innocent ligand either as NO^+, NO or NO^-, availing a series of alternative oxidation state combinations.[10] Furthemore, NO-release in ruthenium-nitrosyl complexes is dependent on the redox potential of the complex and trans-effect of the ligand in trans- position to NO,[11] and NO release can be triggered by one-electron reduction[12] or by photolysis.[13]

Previously, we have already reported the preparation and biological properties of Ru-NO complexes with various aminoacids coordinated in bidentate fashion.[14] All compounds demonstrated only moderate cytotoxicity in a micromolar concentration range against human ovarian carcinoma cells (CH1), which was presumably related to their low lipophilicity and

insufficient intracellular accumulation. In a different series, aminoacids were replaced by more lipophilic azole ligands in trans- and cis-positions to NO ligand, yielding compounds with the general formula (cation)[cis-$RuCl_4$(Hazole)(NO)] and (cation)[trans-$RuCl_4$(Hazole)(NO)].[15] The cytotoxicity of the complexes against CH1 cells varied greatly from submicromolar to high micromolar range. The differences in the cytotoxicity were defined by the azole heterocycle and the most active Ru-NO compounds contained indazole ligands. The contribution of NO in the antiproliferative activity of mono-indazole Ru-NO complexes was not confirmed. However, no external stimuli was applied; therefore, the release of NO in the studied conditions was unlikely.

Inspired by the elevated cytotoxicity of Ru-NO complexes upon the inclusion of indazole ligands into the structure of the complexes, we hypothesized that incorporation of several indazole ligands would result in the augmented intracellular accumulation of Ru-NO complexes and further increase of antiproliferative activity. Since correlation between the number of indazole ligands and the cytotoxicity of the complexes with the general formula $[Ru^{III}Cl_{(6-n)}(indazole)_n]^{(3-n)-}$ was noticed,[16] higher azole-to-chloride ratio could lead to stabilization of lower ruthenium oxidation states, improved cellular uptake and enhancement of antiproliferative activity.

Herein we report on the synthesis of compounds *trans*-$[Ru^{II}(NO_2)_2(Hind)_4]$ (**[2]**), *trans*-$[RuCl(Hind)_4(NO)]Cl_2$ ([**3**]Cl_2), *trans*-$[RuOH(Hind)_4(NO)]Cl_2$ ([**4**]Cl_2), (Scheme 1), their characterization by spectroscopic methods and single crystal X-ray diffraction. Upon characterization of aqueous solution behavior of these complexes, new inner-sphere Ru-NO complexes $[RuCl(ind)_2(Hind)_2(NO)]$ (**5**) and $[RuOH(ind)_2(Hind)_2(NO)]$ (**6**) were isolated and characterized. The redox properties were investigated as well and supporting DFT calculations were performed to assess the IR, UV–vis and EPR behavior of [**3**]Cl_2. The ability of the target complexes [**3**]Cl_2 and [**4**]Cl_2 to release NO upon one-electron reduction or blue light irradiation has been studied by various methods. The contribution of NO to the anticancer properties and p53 induction of novel Ru-NO complexes with or without irradiation has been evaluated.

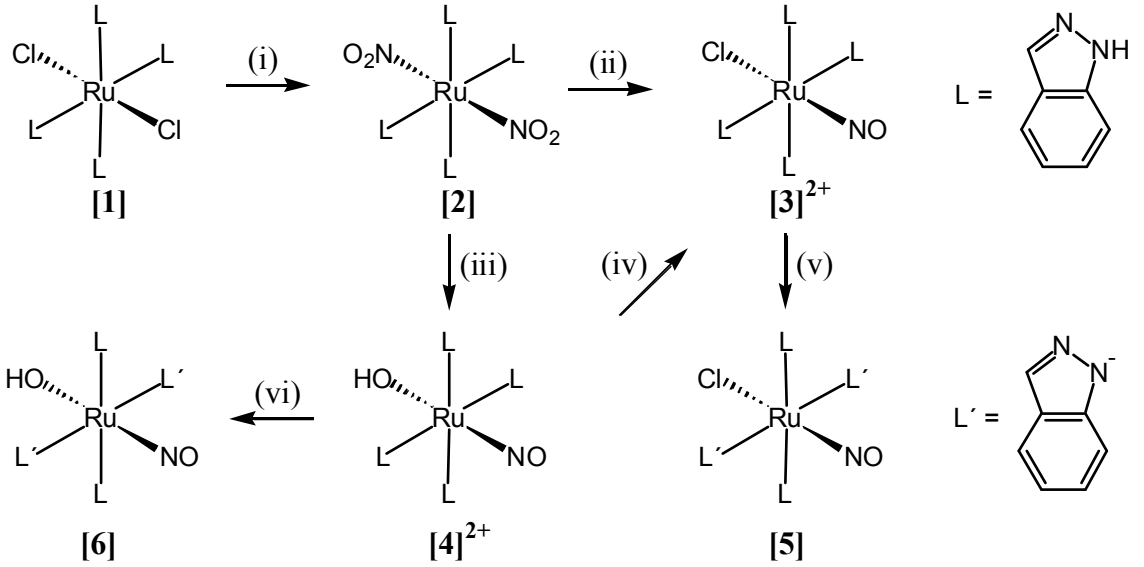

Scheme 1. Synthesis of complexes. Reagents and conditions: (i) $NaNO_2$, acetone/DCM/H_2O reflux, 12 h; (ii) 12M HCl, MeOH; (iii) 3M HCl, MeOH; (iv) 12M HCl, MeOH; (v) and (vi) pH 6–9 in 50% ethanol/water.

Experimental

Chemicals and Materials. Solvents and reagents were obtained from commercial sources and used as received. $[Ru^{II}Cl_2(Hind)_4]$ (**[1]**) was prepared as reported previously.[16] Ultrapure water was obtained by using a Milli-Q UV purification system (Sartorius Stedim Biotech SA). Gibco Trypsin/EDTA solution and 10% sodium dodecyl sulfate (SDS) solution was purchased from Life Technologies. Glycine, HyCloneTM Trypsin Protease 2.5% (10X) solution, RPMI 1640, DMEM medium, Fetal bovine serum (FBS), PierceTM Protease, Phosphatase Inhibitor Mini Tablets and carboxy-PTIO were purchased from Thermo Fisher Scientific. HyCloneTM Dulbecco's Phosphate-Buffered Saline (10 times diluted) was purchased from Ge Healthcare Life Sciences. Biorad Protein Assay Dye Reagent Concentrate, 40% Acrylamide/Bis solution, 10X Tris/glycine buffer, TEMED, Nitrocellulose Membrane 0.2 and 0.45 μm were purchased from Biorad Laboratories. LuminataTM Classico, Crescendo and Forte Western HRP Substrate were purchased from Merck Millipore Corporation. Oxaliplatin was purchased from Merlin Chemicals Ltd (Liphook, UK). Clinical-grade cisplatin (1 mg/ml) was purchased from Hospira Pty Ltd (Melbourne, Australia). All solvents for solution equilibrium studies were of analytical grade and used without further purification. KCl, HCl, HNO_3, KOH, dimethylsulfoxide (DMSO) and other chemicals used were purchased from Sigma-Aldrich in *puriss* quality.

Synthesis of complexes

***trans*-[Ru(NO$_2$)$_2$(Hind)$_4$]] ([2]).** A solution of $NaNO_2$ (0.2 g, 2.6 mmol) in H_2O (8 mL) was added to the mixture of [$RuCl_2$(Hind)$_4$] (0.6 g, 0.93 mmol) in acetone/dichloromethane (DCM) 1:1 (100 mL). The solution was refluxed under stirring for 12 h, and cooled to room temperature. The organic phase was separated in a separatory funnel and washed with water (3 × 30 mL). The volume of the separated organic phase was reduced to ca. 20 ml. After 2 h the precipitated yellow crystals were filtered off, washed with acetone (5 mL) and dried in air. Yield: 0.28 g, 46.0%. X-ray diffraction quality single crystals were grown in DCM/hexane (solvent/vapor diffusion). ^{1}H NMR in DMSO-d_6: 13.32 (s, 4N*H*), 8.09 (s, 4*H*), 7.73 (d, 4*H, J* = 8.5 Hz), 7.61 (d, 4*H, J* = 8.5 Hz), 7.34 (t, 4*H*, *J* = 7.5 Hz), 7.13 (t, 4*H* , *J* = 7.5 Hz). Elem. Anal. Calcd for $C_{28}H_{24}N_{10}O_4Ru$ (M_r = 665.62), %: C, 50.52; H, 3.63; N, 21.04; O, 9.61. Found, %: C, 50.61; H, 3.39; N, 21.12; O, 9.52. ESI-MS in MeOH (negative): *m/z* 665 [Ru(NO$_2$)$_2$(Hind)$_4$]$^-$, 647, 556 541. IR, $\tilde{\nu}$, cm^{-1}: 3303, 3117, 1517, 1469, 1403, 1349, 1257, 1122, 1046, 1026, 755, 602. UV−vis (DCM), λ_{max}, nm (ε, M^{-1} cm^{-1}): 231 (18108), 293 (17513), 325 (21281), 382 (1108).

***trans*-[RuCl(Hind)$_4$NO]Cl$_2$·H$_2$O ([3]Cl$_2$·H$_2$O).** To a suspension of **[2]** (0.17 g, 0.25 mmol) in MeOH (20 mL) a 12M HCl (2.5 mL) was added. The mixture was refluxed under argon for 1 h, and cooled to room temperature. Then the dark-orange solution was filtered and the volume was reduced to ca. 3–5 mL. A small amount of precipitate was removed by filtration and washed with about 10 mL of water. The mother liquor was allowed to crystallize in air at room temperature. Next day the dark-red crystals were filtered off, washed with diethyl ether (10 mL) and dried in vacuo at room temperature (r.t.). Yield: 0.097 g, 52%. Elem. Anal. Calcd for $C_{28}H_{24}Cl_3N_9ORu{\cdot}4H_2O$ (M_r = 782.04), %: C, 43.00; H, 4.12; N, 16.12. Found, %: C, 43.08; H, 3.93; N, 15.91. ESI-MS in MeOH (positive): *m/z* 638 [RuCl(Hind)$_4$(NO)]$^+$. ^{1}H NMR in DMSO-d_6: 14.47 (s), 8,48 (s), 7,92 (d), 7,67 (dd); 7,61 (m), 7,34 (t). IR, $\tilde{\nu}$, cm^{-1}: 2658, 1925 (NO), 1629, 1515, 1476, 1439, 1359, 1288, 1239, 1146, 1088, 999, 966, 902, 840, 783, 737, 614. UV−vis (H_2O), λ_{max}, nm (ε, M^{-1} cm^{-1}): 257 (99175), 365 (53287), 482 (22994). X-ray diffraction quality single crystals were grown in acetone. The monohydrate was obtained by drying the compound in vacuo at room temperature for 8 h.

***trans*-[Ru(OH)(Hind)$_4$(NO)]Cl$_2$·H$_2$O ([4]Cl$_2$·H$_2$O).** To a suspension of **[2]** (0.17 g, 0.25 mmol) in MeOH (20 mL) a 3M HCl (2.5 mL) was added. The mixture was refluxed under argon for 40 min, and cooled to room temperature. Then the dark-orange solution was filtered and the filtrate concentrated under the reduced pressure to ca. 3 mL. The precipitate was

filtered off and washed with water (10 mL). The product was recrystallized from acetone (40 mL), washed with diethyl ether (10 mL) and dried in vacuo at r.t. Yield: 0.11 g, 62%. Elem. Anal. Calcd for $C_{28}H_{25}Cl_2N_9O_2Ru \cdot H_2O$ (M_r = 704.53), %: C, 47.40; H, 3.83; N, 17.77; O, 6.76; Found, %: C, 47.07; H, 3.62; N, 17.57; O, 6.25. ESI-MS in MeOH (positive): *m/z* 620 $[Ru(NO)(OH)(Hind)_4]^+$, 484 $[Ru(Hind)_3]^+$, 310 $[Ru(NO)(OH)(Hind)_4]^{2+}$. ^{1}H NMR in DMSO-$d_6$: 14.27 (br.s, 4N*H*), 8.56 (s, 4*H*), 7.89 (d, 4*H, J* = 8.5 Hz), 7.66 (d, 4*H, J* = 8.5 Hz), 7.56 (t, 4*H, J* = 7.5 Hz), 7.29 (t, 4*H*, *J* = 7.5 Hz). IR, $\tilde{\nu}$, cm^{-1}: 3354, 1879 (NO), 1657, 1585, 1512, 1474, 1441, 1378, 1358, 1334, 1272, 1242, 1151, 1126, 1081, 1003, 964, 830, 784, 746, 656, 619. UV−vis (H_2O), λ_{max}, nm (ε, M^{-1} cm^{-1}): 257 (99175), 365 (53287), 482 (22994). X-ray diffraction quality single crystals were grown in acetone.

***trans,cis,cis*-[RuCl(ind)$_2$(Hind)$_2$(NO)] [5] and [RuOH(ind)$_2$(Hind)$_2$(NO)] [6]**. To a solution of 20 mg of **[3]Cl$_2$**·4H_2O or **[4]Cl$_2$**·H_2O in 8 mL 50% (v/v) ethanol/water 0.1 M KOH solution was added until the measured pH was between 6 and 9. The formed fine-grained precipitate was centrifuged and washed with 50% (v/v) ethanol/water (4 × 4 mL). The product was dried in air. Yield: 50 and 52%, respectively. X-ray diffraction quality single crystals of **[5]·0.8CH$_2$Cl$_2$** were grown in DCM. ^{1}H NMR in $CDCl_3$: [RuCl(ind)$_2$(Hind)$_2$(NO)] **[5]**: 8.04(s), 7,84 (d), 7,69 (d); 7,43 (dd), 7,14 (dd). [Ru(OH)(ind)$_2$(Hind)$_2$(NO)] [**6**]: 7.86(s), 7,78 (d), 7,64 (d); 7,39 (dd), 7,11 (dd); ESI-MS in MeOH (positive): [RuCl(ind)$_2$(Hind)$_2$(NO)] (**[5]**): *m/z* 638 $[M+H]^+$; [RuOH(ind)$_2$(Hind)$_2$(NO)] (**[6]**): *m/z* 620 $[M+H]^+$. IR, $\tilde{\nu}$, cm^{-1} **[5]:** 1871, 1722, 1624, 1509, 1448, 1365, 1095, 733; [**6**]: 1850, 1624, 1583, 1358, 1313, 1075, 783, 747.

Physical Measurements. Elemental analyses were performed by the Microanalytical Service of the Faculty of Chemistry of the University of Vienna with a PerkinElmer 2400 CHN Elemental Analyzer. ^{1}H NMR (500.10 MHz) spectra were measured on a Bruker Avance III instrument at 25 °C. Chemical shifts for ^{1}H were referenced to residual protons present in DMSO-d_6. IR spectra were obtained by using an ATR unit with a Perkin-Elmer 370 FTIR 2000 instrument (4000–400 cm^{-1}). Electrospray ionization mass spectrometry was carried out with a Bruker Esquire3000 instrument (Bruker Daltonics, Bremen, Germany) by using methanol as solvent. Infrared spectroscopy measurements with irradiation were performed using a Nicolet 5700 FT-IR spectrometer with a resolution of 2 cm^{-1} in the range 350–4000 cm^{-1}. The sample was grinded, mixed with KBr, and pressed into pellets. KBr pellets were bonded by silver paste on the cold finger of a closed cycle cryostat (Oxford Optistat V01), and

irradiated through KBr windows with light of different wavelengths in the range 365–660 nm. The cryostat allows controlling the temperature in the range of 9–320 K.

X-ray crystallography. X-ray diffraction measurements were performed on a Bruker X8 APEXII CCD and Bruker D8 Venture diffractometers. Single crystals were positioned at 35, 40 35 and 28 mm from the detector, and 767, 1872, 1904 and 2500 frames were measured, each for 30, 2, 7.2 and 48 s over 1, 0.25, 0.4 and 0.5° scan width for **[2]**, **[3]Cl_2·2$(CH_3)_2CO$**, **[4]Cl_2·2$(CH_3)_2CO$** and **[5]·0.8CH_2Cl_2**, respectively. The data were processed using SAINT software.[47] Crystal data, data collection parameters, and structure refinement details are given in Table S1. The structure was solved by direct methods and refined by full-matrix least-squares techniques. Non-hydrogen atoms were refined with anisotropic displacement parameters. Hydrogen atoms were inserted in calculated positions and refined with a riding model. The following computer programs and hardware were used: structure solution, *SHELXS-97* and refinement, *SHELXL-97*;[48] molecular diagrams, ORTEP;[49] computer, Intel CoreDuo. Disorder observed for the nitro group in **[2]** and two indazole, NO and OH ligands in **[3]**$^{2+}$ was resolved by using SADI and EADP restraints and DFIX constraints implemented in SHELXL. Crystallographic data for these complexes have been deposited with the Cambridge Crystallographic Data Center as supplementary publications no. CCDC-1835290 (**[2]**), -1835292 (**[3]Cl_2·2$(CH_3)_2CO$**), -1835291 (**[4]Cl_2·2$(CH_3)_2CO$**), and -1835289 (**[5]·0.8CH_2Cl_2**). Copy of the data can be obtained free of charge on application to The Director, CCDC, 12 Union Road, Cambridge CB2 1EZ, UK (email: deposit@ccdc.cam.ac.uk).

Solution equilibrium studies. Aqueous stability and proton dissociation processes of complexes **[3]Cl_2** and **[4]Cl_2** were investigated in detail. Due to the photosensibility of the complexes their solutions were kept in dark. A Hewlett Packard 8452A diode array spectrophotometer was used to record the UV–vis spectra in the interval 200–800 nm. The path length was 0.2, 0.5, 1 or 4 cm. Spectrophotometric measurements were performed in water, 50% (v/v) ethanol/water or 30% (v/v) DMSO/water solvent mixtures at 25.0±0.1 °C and the concentration of the complexes was 4–5 or 100 μM. The ionic strength was 0.1 M (KCl). Measurements in chloride ion free media were carried out as well in the presence of HNO_3 (pH ~ 3) without additional background electrolyte. pH dependent titrations were performed between pH 2.0 and 11.5 and an Orion710A pH-meter equipped with a Metrohm combined electrode (type 6.0234.100) was used for the titrations. The electrode system was calibrated in aqueous solution to the pH = –log[H^+] scale according to the method suggested

by Irving et al.[17] ^{1}H NMR studies were carried out on a Bruker Ultrashield 500 Plus instrument. ^{1}H NMR spectra of samples containing water were recorded with the WATERGATE water suppression pulse scheme using 4,4-dimethyl-4-silapentane-1-sulfonic acid (DSS) internal standard. Complexes were dissolved in 50% (v/v) CD_3OD/H_2O mixture to yield a concentration of 0.5 mM and were titrated at 25 °C, in the absence of KCl in the pH range 2.0 to 11.1. ^{1}H NMR spectra were recorded on samples containing **[4]Cl$_2$** (0.5 mM) and increasing amount of KCl (0.0, 0.44, 0.68 M) after 2 h of incubation. Fluorescence spectra were recorded on a Hitachi-F4500 fluorometer in 1 cm quartz cell at λ_{EX} = 290 nm, λ_{EM} = 300–500 nm and at 25.0 ± 0.1 °C. Solutions were prepared in pure water at 5 μM complex concentration. Ionic strength was 0.1 M (KCl), and samples were titrated between pH 2.0 and 11.5.

Electrochemistry and Spectroelectrochemistry. The cyclic voltammetric studies were performed using a platinum wire as working and auxiliary electrodes, and silver wire as pseudoreference electrode with a Heka PG310USB (Lambrecht, Germany) potentiostat. Ferrocene served as the internal potential standard. *In situ* spectroelectrochemical measurements were performed on Avantes, Model AvaSpec-2048x14-USB2 spectrometer under an argon atmosphere with the Pt-microstructured honeycomb working electrode, purchased from Pine Research Instrumentation (spectroelectrochemical cell kit AKSTCKIT3). IR spectroelectrochemistry was performed in the optically transparent thin layer electrochemical (OTTLE) cell (UF-SEC, LabOmak, Italy) with CaF_2 windows and Pt mesh working electrode. Spectra were recorded at room temperature in the 400–4000 cm^{-1} with 4 cm^{-1} resolution using Nicolet NEXUS 470 FT-IR spectrometer. Further details are provided in the SI.

EPR spectroscopy. X-band (9.4 GHz) and Q-band (34 GHz) EPR spectra were recorded with the EMX line EPR spectrometers (Bruker, Germany) equipped with the ER 4102ST and ER 5106 QT resonators, respectively and with the ER 4141 VT variable temperature unit. The simulated spectra were calculated with EasySpin, the Matlab toolbox [18]. Further details are provided in the SI.

Solution photochemistry in minutes time scale. NO scavenging EPR experiments were performed with 33 μM solution of [**3**]Cl_2 and an equimolar concentration of carboxy-2-phenyl-4,4,5,5-tetramethyl-imidazoline-1-oxyl-3-oxide (cPTIO) nitronyl nitroxide in Ar saturated MeCN. The solution was filled in an EPR flat cell and irradiated *in situ* in the resonator of the EPR spectrometer described above at room temperature with a vis light

source (λ_{max} = 400 nm; Bluepoint LED, Hönle UV Technology). The photolysis of 30–35 μM stirred complex solutions was additionally followed by UV–vis spectroscopy *in situ* in the LED photoreactor equipped with two λ_{max} = 365 or 405 nm LED arrays (KEVA Brno, Czech Republic), in a perpendicular arrangement using 1 cm×1 cm quartz cuvette (1 cm optical irradiation path). The UV–vis Avantes spectrometer described above was used to record the spectra. The light intensity provided by the LED arrays (irradiance value) was determined using ferrioxalate actinometry under identical conditions (yielding 7.81×10^{-4} einstein s^{-1} dm^{-3} and 1.18×10^{-4} einstein s^{-1} dm^{-3} at 365 nm and 405 nm, respectively).[19] The spectra were corrected for the irradiation light artefacts, by subtracting a record obtained with the pure solvent. The molar absorption coefficient of the photo generated products and the photochemical quantum yields were determined by kinetic modeling. The Global Analysis of the spectral series recorded in the photolysis experiment was performed using the Ultrafast Spectroscopy Modelling Toolbox,[20] by employing a first order kinetic model. The rate constants and concentration profiles obtained were then used to evaluate the quantum yield as described in the text.

Femtosecond Pump-Probe Spectroscopy. The experimental details for the femtosecond transient absorption measurements have already been described elsewhere.[21] Briefly it is a Ti:Sapphire laser (Mai Tai HP, Spectra Physics, USA) centered at 800 nm having pulse width of < 110 fs with 80 MHz repetition rate. The amplified laser was split into two beams in the ratio of 75:25%. The high energy beam was used to convert to the required wavelength (470 nm) for exciting the sample by using TOPAZ (Prime, Light Conversion). The white light continuum (340–1000 nm) was generated by focusing the part of amplified beam (200 mW) on a 1 mm thick CaF_2 plate which split into two beams (sample and reference probe beams). The sample cell (0.4 mm path length) was refreshed by rotating in a constant speed. Finally, the white light continuum was focused into a 100 μm optical fiber coupled to imaging spectrometer after passing through the sample cell. The pump probe spectrophotometer (ExciPro) setup was purchased from CDP Systems Corp, Russia. Normally transient absorption spectra were obtained by averaging about 2000 excitation pulses for each spectral delay. All the measurements were carried out at the magic angle (54.7°). The time resolution of the pump-probe spectrometer is found to be about ≤ 120 fs.

Computational details. Geometry optimizations of all studied species of $[\mathbf{3}]^{2+}$ (i.e $[RuCl(Hind)_4(NO)]^{2+}$, its reduced form ,$^2[RuCl(Hind)_4]^{2+}$ form after NO release, *etc*.) have been performed at the B3LYP[22,23,24,25] level of theory employing SVP and/or TZVP basis

sets[26] with SDD pseudopotential for the Ru atom.[27] The energy-based criterion of the SCF convergence was set to 10^{-8} Hartree in all systems. Vibrational analysis was employed to confirm that the optimal geometries correspond to energy minima (no imaginary frequencies). Time-dependent density functional theory (TD DFT) has been utilized for calculations of electron excitation energies and oscillator strengths at the same levels of theory as mentioned above. Herein, the forty lowest electron excitations have been taken into account. All these calculations were carried out in Gaussian09 program package.[28] The single point calculations of EPR parameters of the optimized structures were performed at the B3LYP[22,23,24,25]/UDZ[29] level of theory in ORCA 3.0.2 program package,[30,31,32] where UDZ stands for uncontracted double zeta basis set. The EPR calculations employed a scalar quasirelativistic Douglas-Kroll-Hess Hamiltonian[30,33,34,35,36] with the unrestricted Kohn-Sham formalism and using the point charge nucleus model. Picture change error[37] correction of the *g*-tensor and hyperfine coupling constant of N3 atom was accounted for as implemented in the ORCA 3.0.2 program package. Visualization of the optimal structures and molecular orbitals as well as spin densities was performed in Molekel[38] software suite.

Cell lines and culture conditions. Human colorectal carcinoma HCT116 and HCT116 p53-/- cell lines were gifts from Professor Shen Han-ming (NUS). Human ovarian carcinoma cells A2780 and human embryonic kidney cells HEK293 were obtained from ATCC. A2780 cells were cultured in RPMI 1640 medium containing 10% fetal bovine serum (FBS). HCT116 and HEK293 were cultured in DMEM medium containing 10% FBS. Adherent cells were grown in tissue culture 25 cm^2 flasks (BD Biosciences, Singapore). All cell lines were grown at 37 °C in a humidified atmosphere of 95% air and 5% CO_2. Experiments were performed on cells within 30 passages. All drug stock solutions were prepared in DMSO and the final concentration of DMSO in medium did not exceed 1% (v/v) at which cell viability was not inhibited. The amount of actual Ru concentration in the stock solutions was determined by ICP-OES.

Inhibition of cell viability assay. The cytotoxicity of the compounds was determined by colorimetric microculture assay (MTT assay). The cells were harvested from culture flasks by trypsinization and seeded into Cellstar 96-well microculture plates (Greiner Bio-One) at the seeding density of 6×10^3 cells per well. After the cells were allowed to resume exponential growth for 24 h, they were exposed to drugs at different concentrations in media for 72 h. The drugs were diluted in complete medium at the desired concentration and 100 μL of the drug solution was added to each well and serially diluted to other wells. After exposure for 72 h,

drug solutions were replaced with 100 μL of MTT in media (5 mg mL^{-1}) and incubated for additional 45 min. Subsequently, the medium was aspirated and the purple formazan crystals formed in viable cells were dissolved in 100 μL of DMSO per well. Optical densities were measured at 570 nm with a microplate reader. For cell viability assays involving inhibitors, the cells were pre-incubated with pifithrin-α (10 μM) or carboxy-PTIO (2.5 or 10 μM) for 30 min and then co-incubated with drugs for 72 h. Cell viability in the absence and presence of inhibitor was normalized against untreated control. For the irradiation experiments, drug stock solutions were prepared in MeCN and their concentrations were independently verified by ICP-OES. The concentration of MeCN in medium did not exceed 1% (v/v) at which cell viability was not inhibited. Drug stock solutions were irradiated by 18 W blue LED strips (maximum emission at around 470 nm) for 5 min and quickly diluted in complete medium at the desired concentration and MTT assay was carried out as described. The irradiation of drug solutions was characterized by the appearance of blue color. The quantity of viable cells was expressed in terms of treated/control (T/C) values by comparison to untreated control cells, and 50% inhibitory concentrations (IC_{50}) were calculated from concentration-effect curves by interpolation. Evaluation was based on means from at least three independent experiments, each comprising six replicates per concentration level.

Western blot analysis. A2780 cells were seeded into Cellstar 6-well plates (Greiner Bio-One) at a density of 6×10^5 cells per well. After the cells were allowed to resume exponential growth for 24 h, they were exposed to **[1]**, **[3]Cl_2**, **[4]Cl_2**, cisplatin and oxaliplatin at different concentrations for 24 h. The cells were washed twice with 1 mL of PBS and lysed with lysis buffer [100 μL, 1% IGEPAL CA-630, 150 mM NaCl, 50 mM Tris-HCl (pH 8.0), protease inhibitor] for 5–10 min at 4 °C. The cell lysates were scraped from the wells and transferred to separate 1.5 mL microtubes. The supernatant was then collected after centrifugation (13000 rpm, 4 °C for 15 min) and total protein content of each sample was quantified *via* Bradford's assay. Equal quantities of protein (50 μg) were reconstituted in loading buffer [5% DDT, 5× Laemmli Buffer] and heated at 105 °C for 10 min. Subsequently, the protein mixtures were resolved on a 10% SDS-PAGE gel by electrophoresis (90 V for 30 min followed by 120 V for 60 min) and transferred onto a nitrocellulose membrane (200 mA for 2 h). The protein bands were visualized with Ponceau S stain solution and the nitrocellulose membranes were cut into strips based on the protein ladder. The membranes were washed with a wash buffer (0.1% Tween-20 in 1× DPBS) three times for 5 min. Subsequently, they were blocked in 5% (w/v) non-fat milk in wash buffer (actin and p53 antibodies) or 5% BSA (w/v) in wash buffer (p21

antibody) for 1 h and subsequently incubated with the appropriate primary antibodies in 2% (w/v) non-fat milk in wash buffer (actin and p53 antibodies) or 5% BSA (w/v) in wash buffer (p21 antibody) at 4 °C overnight. The membranes were washed with a wash buffer 3 times for 7 min. After incubation with horseradish peroxidase-conjugated secondary antibodies (r.t., 1.5 h), the membranes were washed with a wash buffer 4 times for 5 min. Immune complexes were detected with Luminata HRP substrates and analyzed using enhanced chemiluminescence imaging (PXi, Syngene). Actin was used as a loading control. The following antibodies were used: p53 (FL-393) (sc-6243) and p21 (F-5) (sc-6246) from Santa Cruz Biotechnologies, β-Actin (ab75186) from Abcam, ECL.

Results and Discussion

Synthesis of complexes. The complexes *trans*-[RuCl(Hind)$_4$(NO)]Cl$_2$·H$_2$O (**[3]Cl$_2$·H$_2$O**), *trans*-[RuOH(Hind)$_4$(NO)]Cl$_2$·H$_2$O (**[4]Cl$_2$·H$_2$O**), [RuCl(ind)$_2$(Hind)$_2$(NO)] (**[5]**) and [RuOH(ind)$_2$(Hind)$_2$(NO)] (**[6]**) were synthesized as shown in Scheme 1. Metathesis reaction of *trans*-[RuCl$_2$(Hind)$_4$] (**[1]**) with a 50% molar excess of NaNO$_2$ afforded the complex *trans*-[Ru(NO$_2$)$_2$(Hind)$_4$] (**[2]**) in 46% yield. Treatment of the latter with 12M and 3M HCl in methanol resulted in formation of **[3]Cl$_2$·H$_2$O** and **[4]Cl$_2$·H$_2$O** in 52 and 62%, respectively. These two compounds were found to deprotonate at pH 6–9 (*vide infra*) with formation of **[5]** and **[6]**, in ca 50% yield. By reacting **[4]Cl$_2$** with 12M HCl a conversion into **[3]Cl$_2$** was observed, even though it was not complete. The composition and structure proposed for all new compounds reported in this work have been proposed from elemental analyses, ^{1}H NMR, IR and UV–vis spectra, ESI mass spectrometry (see Experimental Section) and confirmed by single crystal X-ray diffraction measurements (vide infra). It should, however, be noted that the compounds used in all investigations described below are anhydrous or hydrated compounds (see Experimental section), while those characterized by single crystal X-ray diffraction are either anhydrous or contain co-crystallized solvent used for crystal growth.

X-ray Crystallography. The results of X-ray diffraction studies of complexes **[2]**, **[3]Cl$_2$·2(CH$_3$)$_2$CO), [4]Cl$_2$·2(CH$_3$)$_2$CO)** and **5·0.8CH$_2$Cl$_2$** are shown in Figure S1 and Figure 1, details of data collection and refinement are given in Table S1, while selected bond lengths (Å) and angles (deg) are quoted in the legends to Figures S1 and 1. Complex **[2]** crystallized in the tetragonal space group $I4_1/a$, while the other three compounds in monoclinic space group $P2_1/n$ (or $P2_1/c$) (Table S1). All four complexes adopt a distorted octahedral coordination geometry with four indazole ligands coordinated to ruthenium in equatorial

plane and two nitrito groups (**[2]**), NO and chlorido (**[3]Cl$_2$**) and [**5**] or NO and hydroxido (**[4]Cl$_2$**) as axial ligands. Interestingly, in **[5]** two adjacent indazole ligands are deprotonated at N6 and N8 acting as proton acceptors in intramolecular hydrogen bonds N4–H···N6 [N4···N6 2.800(2) Å, N4–H···N6 170°] and N2–H···N8 [N2···N8 2.800(2) Å, N2–H···N8 170°] (Figure 1C).

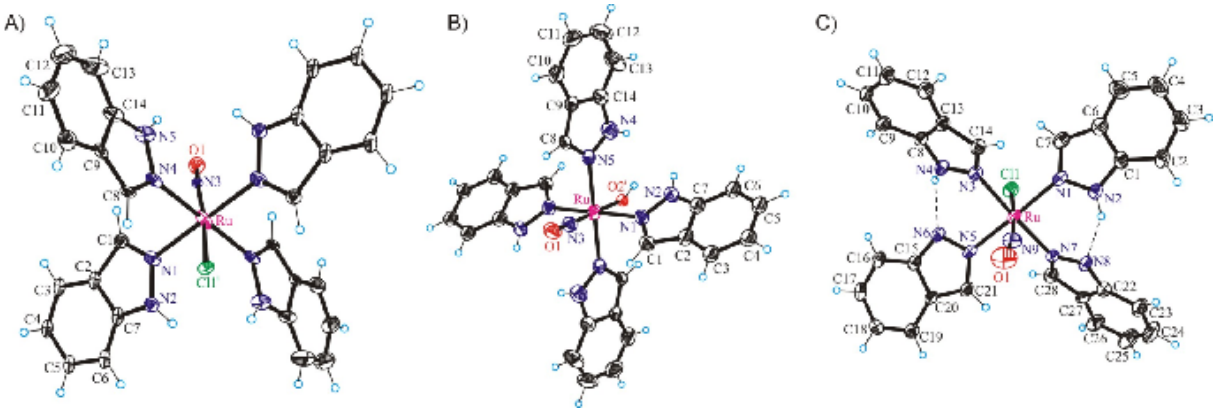

Figure 1. A) ORTEP view of the cation $[RuCl(NO)(Hind)_4]^{2+}$ in the crystal structure of **[3]Cl$_2$·2(CH$_3$)$_2$CO)** with atom labeling scheme and thermal ellipsoids at 50% probability level; only the major components of the disordered over two positions Cl^- and NO are shown. Counterions and solvent molecules in the crystal structure are omitted for clarity. Selected bond distances (Å) and angles (deg): Ru–N1 2.080(6), Ru–N4 2.085(7), Ru–Cl1^i 2.214(7), Ru–N3 1.806(19), N3–O1 1.174(19), Ru–N3–O1 168.9(17), Cl1^i–Ru–N3 174.5(6); B) ORTEP view of the cation $[Ru(OH)(NO)(Hind)_4]^{2+}$ in the crystal structure of **[4]Cl$_2$·2(CH$_3$)$_2$CO)** with atom labeling scheme and thermal ellipsoids at 50% probability level; only the major components of the disordered over two positions OH^-, NO and two indazole ligands are shown. Counterions and solvent molecules in the crystal structure are omitted for clarity. Selected bond distances (Å) and angles (deg): Ru–N1 2.078(3), Ru–N4 2.078(3), Ru–O2^i 1.996(9), Ru–N3 1.702(11), Ru–N3–O1 171.0(9), N3–Ru–O2^i 178.1(6); C) ORTEP view of the neutral complex $[RuCl(ind)_2(Hind)_2(NO)]$ [**5**] with atom labeling scheme and thermal ellipsoids at 50% probability level. Co-crystallized solvent is omitted for clarity. Selected bond distances (Å) and angles (deg): Ru–N1 2.090(4), Ru–N3 2.094(4), Ru–N5 2.081(4), Ru–N7 2.073(4), Ru–Cl1 2.2959(13), Ru–N9 1.774(5), N9–O1 1.127(6), Ru–N9–O1 168.7(5), N9–Ru–Cl1 174.68(15).

Note that X-ray diffraction structures of complexes with deprotonated indazole are rare in the literature. Two examples can be mentioned, namely the platinum complex $[PtCl(N\text{-indazolato})(PPh_3)_2]$[39] and the osmium-arene complex [(η^6-*p*-cymene)Os(oxine)(ind)].[40] The Ru–NO moiety is almost linear with the corresponding angle varying from 168.7(5)° to 171.0(9)°. In addition to X-ray diffraction data the linear geometry of Ru–NO unit in **[3]Cl$_2$**,

[4]Cl_2, **[5]** and **[6]** was also obvious from IR spectra, where strong absorption bands with ν_{NO} at 1925, 1879, 1871 and 1850 cm^{-1} were measured. Therefore, the photoreactivity of this moiety in the solid state was first investigated.

Solid state photochemistry. In metal nitrosyl complexes sometimes a competition between NO release and the generation of photoinduced NO linkage isomers (PLI) exists. These PLI were first discovered in $Na_2[Fe(CN)_5(NO)]$,[41,42] and termed long-lived metastable states (MS). Since then a number of ruthenium complexes have been prepared with similar photophysical behavior.[43,44,45,46,47] In order to evaluate the ability of the reported herein complexes to form PLI and/or release NO we performed a systematic analysis by infrared spectroscopy as a function of temperature, which are detailed in Supporting Information material (Figures S2–S4). In summary, upon light irradiation solid **[3]Cl_2·H_2O** did not exhibit significant metastable isomer population, but considerable NO release at room temperature. In contrast, for **[4]Cl_2·H_2O** and **[5]** we observed both phenomena NO release at room temperature and linkage isomerism at low temperature, which in case of **[5]** is reversible.

Solution chemistry of complexes [3]Cl_2 and [4]Cl_2 in aqueous media. Structural and spectroscopic characterization of compounds is usually performed in the solid state or in organic solvents. However, for the drug development it is important to collect the information about the stability and reactivity of the drug candidates in aqueous media, especially at physiological pH. It is known that pH in solid tumors is usually lower than in normal tissues and acidosis in cancer cells is mediated by glycolysis, induced by limited oxygen supply.[48] Typical extracellular pH ranges are 6.5–6.9 in tumors and 7.0–7.5 in normal tissues; however, in some tumors pH values of 6.0 or even lower were detected.[49] Therefore, the behavior of drug candidates should also be assessed at acidic conditions. Complexes [**3**]Cl_2 and [**4**]Cl_2 may participate in several interactions in aqueous media. Besides the (partial) decomposition of the complexes (*i.e.* loss of NO or Hind ligands, Cl^-/OH^- exchange), protonation of the coordinated OH^- in [**4**]Cl_2 or stepwise deprotonation of Hind ligands in both complexes **[3]Cl_2** and **[4]Cl_2** may take place in aqueous solution by varying the pH as it is shown in Scheme 2 for $[\mathbf{4}]^{2+}$.

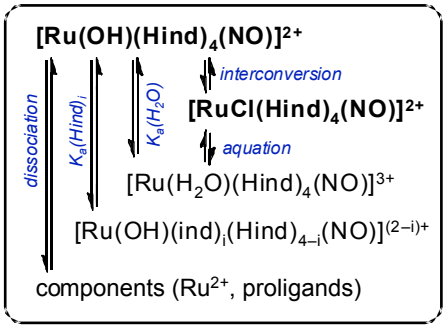

Scheme 2. Possible transformation processes of $[Ru(OH)(Hind)_4(NO)]^{2+}$ ($\mathbf{[4]^{2+}}$) including interconversion to $[RuCl(Hind)_4(NO)]^{2+}$ ($\mathbf{[3]^{2+}}$) and aquation of the latter as well. The same protonation and dissociation equilibria are valid for $\mathbf{[3]^{2+}}$.

Chlorido ligand often behaves as a leaving group, especially in the case of platinum-group metal complexes.[50,51,52] Correct interpretation of the actual form of a compound at physiological conditions requires detailed investigations under variation of different parameters (pH, ionic strength *etc.*) in aqueous media.

The aqueous solubility of complexes $\mathbf{[3]Cl_2}$ and $\mathbf{[4]Cl_2}$ at pH 7.4 was extremely poor and precipitate formation was observed even at 5 μM complex concentration, thereby hindering their detailed investigation in neat water at this pH due to the concentration requirements of the chosen experimental methods. The aqueous solubility increased under acidic conditions (pH 2–4) but was still limited (~100 μM). Due to the low solubility of $\mathbf{[3]Cl_2}$ and $\mathbf{[4]Cl_2}$ in water, their solution chemistry was investigated in 30% (v/v) DMSO/water or 50% (v/v) ethanol/water solvent mixtures. First, the interconversion between the two complexes was investigated. UV–vis spectra recorded in 50% (v/v) ethanol/water or 30% (v/v) DMSO/water mixture showed different spectral shapes at pH 2.3 (Figure S5) and spectra remained unaltered over 1 h. ^{1}H NMR spectra measured for $\mathbf{[4]Cl_2}$ at various KCl concentrations (0–0.68 M) in 50% (v/v) CD_3OD/water at pH = 4.9 provide further evidence that no Cl^-/H_2O or Cl^-/OH^- exchange occurred after incubation for 2 h (Figure S6). The same conclusion can be drawn from ESI-MS measurements: mass spectra of $\mathbf{[3]Cl_2}$ and $\mathbf{[4]Cl_2}$ showed the exclusive presence of the original complexes in the samples even after 8 days incubation in diluted nitric acid (pH ~ 3), accordingly no aquation of $\mathbf{[3]Cl_2}$, no interconversion and no decomposition of the complexes occur in aqueous media. Next, we studied the behavior of complexes $\mathbf{[3]Cl_2}$ and $\mathbf{[4]Cl_2}$ upon pH increase from ≈2 to ≈11 in 50% ethanol/water by UV–vis. As shown in Figure 2A considerable changes in charge transfer bands occur in UV–vis spectra of $\mathbf{[4]Cl_2}$ at pH 2.2–5.3, while practically no measurable changes were observed for the chlorido complex $\mathbf{[3]Cl_2}$ in this pH range (see Figure S7). This

may be explained by the protonation of OH^- in **[4]Cl$_2$** at more acidic conditions resulting in the formation of the aqua complex $[Ru(H_2O)(Hind)_4(NO)]^{3+}$.

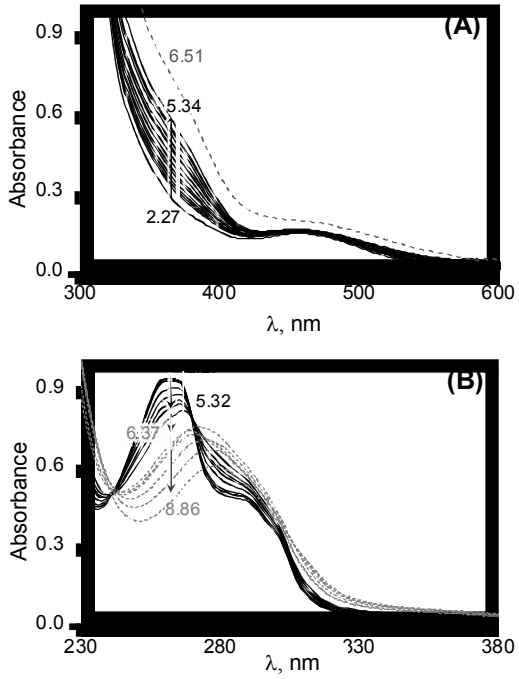

Figure 2. Visible (A) and UV (B) spectra of **[4]Cl$_2$** recorded at various pH values in 50% (v/v) ethanol/water. Dashed spectra indicate precipitate formation, pH values are indicated in the figure. {$c_{complex}$ = 102 μM (A), 5.1 μM (B); l = 4 cm, I = 0.1 M KCl}

At pH above 5.3 intraligand bands of **[4]Cl$_2$** in Figure 2B show significant spectral changes indicating the involvement of Hind ligands into a pH dependent process. To assess if the incubation of complexes **[3]Cl$_2$** and **[4]Cl$_2$** at different pH was associated with the release of indazole ligands, ^{1}H NMR spectra at different pH in 50% CD_3OD/water were recorded. **[4]Cl$_2$** demonstrated high field shifts of proton signals at pH above 5 in Figure 3, but no free indazole could be detected at any pH ruling out the release of indazole from the complex.

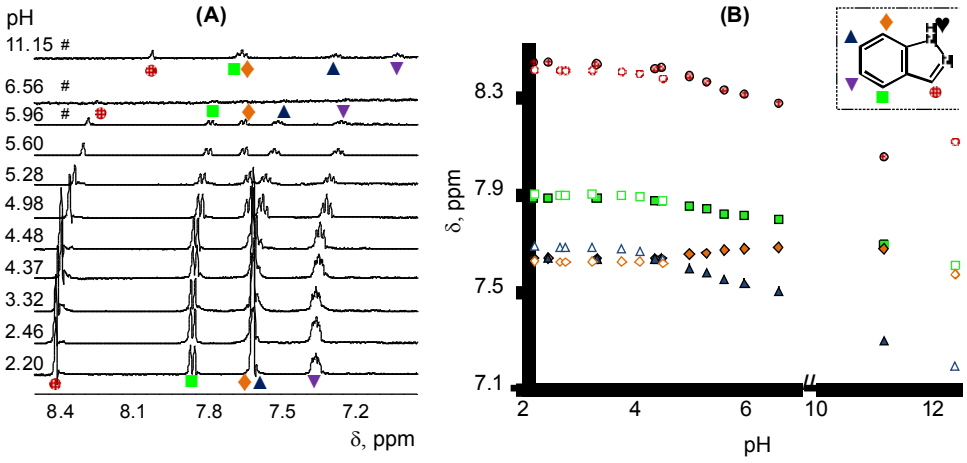

Figure 3. ^{1}H NMR spectra of **[4]Cl$_2$** recorded at various pH values (A) and chemical shift values (δ) of **[3]Cl$_2$** (empty symbols) and **[4]Cl$_2$** (full symbols) plotted against the pH. {$c_{complex}$ = 0.5 mM; 50% (v/v) CD_3OD/water} #: magnified spectral intensities.

This assumption was supported by spectrofluorimetric experiments, which indicated high stability of Ru-Hind bond (Figure S8). The proton shifts of coordinated indazole signals in ^{1}H NMR upon pH changes were associated with indazole deprotonation. Increase of pH above 6.5 was accompanied by precipitation of both complexes with partial redissolution at pH ≈ 11. Complexes **[3]Cl$_2$** and **[4]Cl$_2$** were found to deprotonate with the formation of [RuCl(ind)$_2$(Hind)$_2$(NO)] (**[5]**) and [RuOH(ind)$_2$(Hind)$_2$(NO)] (**[6]**), respectively. The solid-state structure of **[5]** was confirmed by X-ray diffraction analysis (Figure 1C, *vide supra*). To conclude, solution studies revealed the high aqueous stability (or kinetic inertness) of both complexes. Thus, Hind ligands underwent stepwise deprotonation in **[3]Cl$_2$** and **[4]Cl$_2$** resulting in the charge neutral complexes **[5]** and **[6]**, respectively at physiological pH. However, the low solubility of these species at physiological pH hindered further investigation of their aqueous behavior and biological activity.

Electrochemical and spectroscopic studies. Redox properties of the ruthenium nitrosyl complexes have been characterized in organic solvents since, these media provide a considerably larger potential windows for electrochemical investigations, compared to aqueous environment. The first reduction step for *trans*-[RuCl(Hind)$_4$(NO)]$^{2+}$ (**[3]$^{2+}$**) in a 0.2 M *n*Bu$_4$NPF$_6$/MeCN is electrochemically reversible with $E_{1/2}$ = –0.11 V vs Fc^+/Fc (Figure S9A) and is followed by the less reversible one at $E_{1/2}$ = –0.80 V vs Fc^+/Fc. Notably, a very similar behavior was reported for a number of other ruthenium nitrosyl complexes suggesting that redox events mainly involve the NO ligand, namely the reduction of formal Ru^{II}-NO^+ to Ru^{II}-$NO^{\bullet}$ in the first step and the Ru^{II}-$NO^{\bullet}$ transformation to the Ru^{II}-NO^- in the next step.[53] Cyclic voltammogram of *trans*-[Ru(OH)(Hind)$_4$(NO)]$^{2+}$ (**[4]$^{2+}$**) in a 0.2 M *n*Bu$_4$NPF$_6$/MeCN shows the first reduction peak at E_{pc} = –0.47 V vs Fc^+/Fc at scan rate of 100 mV s^{-1} and a strongly shifted reoxidation peak at E_{pa} = –0.08 V vs Fc^+/Fc. The second electron transfer occurs at E_{pc} = –0.8 V vs Fc^+/Fc (Figure S9B). Similar redox behavior for **[4]$^{2+}$** was observed also in dichloromethane (DCM) and ethanol solutions (Figure S10). The one-electron reduction for **[3]$^{2+}$** was confirmed by coulometric measurements and is in line with the reduction of either *trans*-[Ru^{III}Cl(Hind)$_4$(NO^0)]$^{2+}$ or *trans*-[Ru^{II}Cl(Hind)$_4$(NO^+)]$^{2+}$ to the corresponding monocation, which can be formulated as *trans*-[Ru^{II}Cl(Hind)$_4$(NO^0)]$^+$ (**[3]$^+$**).

The latter is a paramagnetic species of $\{Ru(NO)\}^7$ type according to the Enemark-Feltham notation.[54] The formation of paramagnetic $\{Ru(NO)\}^7$ species upon one-electron reduction was also confirmed for deprotonated analogues **[5]** and **[6]** by EPR spectroscopy, even though the first cathodic step is less electrochemically reversible (Figure S11).

The parent **[3]Cl$_2$** and **[4]Cl$_2$**, were found to be EPR silent both in the solid state, as well as in the frozen solutions at 100 K. For both electrochemically generated **[3]**$^+$ and **[4]**$^+$ cations a characteristic $\{Ru(NO)\}^7$ EPR signal, featuring a rhombic g tensor ($g_1 > 2$, $g_2 \approx 2.0$, $g_3 < 2$) and a well-resolved nitrogen hyperfine splitting in the g_2 range ($A_2 \approx 92$ MHz or 3.3 mT), was observed (Figure S12A).[55,56] Annealing of the **[4]**$^+$ sample up to 220 K resulted in a progressive line broadening, and collapse of the resolved features into a single broad singlet (Figure S12B). These results are in line with the formulation of a closed shell $\{Ru(NO)\}^6$ state containing Ru^{II} ($S = 0$) bonded to NO^+ ($S = 0$) for the parent complexes **[3]**$^{2+}$ or **[4]**$^{2+}$. The reduction of the complexes then results in $\{Ru(NO)\}^7$ ($S = ½$) species, which bears an unpaired electron and shows EPR activity.[57] The rather positive value of the first reduction potential of **[3]**$^{2+}$ offers an alternative method for convenient generation of the paramagnetic one-electron reduced species **[3]**$^+$ by using decamethyl ferrocene (Fc*) as reductant. The X- and Q-band EPR spectra of frozen solutions of **[3]**$^+$, prepared in this manner, are shown in Figure S13A,B, respectively. The EPR spectra obtained by chemical reduction in MeCN/nBu$_4$NPF$_6$ solutions (black lines in Figure S13A,B) perfectly matched the records of electro-generated **[3]**$^+$. The X-band EPR signal of **[3]**$^+$ resembles well the spectra of several $\{Ru(NO)\}^7$ systems known from the literature, e.g., the extensively studied porphyrin complexes [Ru(OEP)(NO)(THF)],[58] [Ru(OEP)(NO)(py)][59] or [(TPP)Ru(NO)(py)].[60] The reduction with Fc* was also successfully used to generate the one electron reduced $\{Ru(NO)\}^7$ species from **[4]**$^{2+}$, **[5]**^{0} and **[6]**^{0}. Their EPR spectra are summarized in Figures S13–S20 and the estimated Spin Hamiltonian parameters are listed in Table S2. By simulation of the corresponding EPR spectra two components were taken into account (see discussion in SI, Figures S15–S17 and Table S2). The major component can be clearly assigned to the authentic species **[3]**$^+$ and **[4]**$^+$. Detailed analysis of the minor component is beyond the scope of this paper and further detailed experimental and theoretical studies are currently underway in one of our laboratories.

The reversibility and redox mechanism in the region of the first reduction peak for **[3]**$^{2+}$ and **[4]**$^{2+}$ were investigated by the *in situ* spectroelectrochemical UV–vis cyclic voltammetric experiments in MeCN/nBu$_4$NPF$_6$. Upon the *in situ* reduction of **[3]**$^{2+}$ at a scan

rate of 10 mV s^{-1}, in the region from +0.15 to –0.51 V vs Fc^+/Fc, the UV–vis absorption bands at 260 nm (strong absorption) and 460 (weak absorption) decreased, and, simultaneously, a new optical band at 360 nm emerged (Figure 4A). Fully reversible spectroelectrochemical behavior confirmed the high stability of cathodically generated monocation $\mathbf{[3]}^+$ (see response for the two consecutive CV scans in Figure 4B). Difference optical spectra (taking the initial sample solution spectrum as the reference) are shown for clarity since the transformations of the low intensity bands are easier to follow in this case (absolute spectra are shown in Figure S21). Similar spectroelectrochemical response was observed for $\mathbf{[4]}^{2+}$ (Figure S22). The potential dependence of UV–vis spectra measured for the two consecutive cyclic voltammetric scans in thin layer cell is shown in Figure S22B. Upon the *in situ* reduction of $\mathbf{[4]}^{2+}$ in MeCN at a scan rate of 10 mV s^{-1} in the region from +0.3 to –0.6 V vs Fc^+/Fc, the UV–vis absorption band at 264 nm decreased, while a new optical bands at 284 and ca. 360 nm via an isosbestic point at 272 nm appeared (Figure S22C). The isosbestic points in the forward and the reverse voltammetric scans (Figure S22C,D) indicate the chemical reversibility of the first reduction step and the stability of the paramagnetic reduced species $[\mathbf{4}]^+$.

The IR spectra recorded upon the one electron reduction of $\mathbf{[3]}^{2+}$ showed a decrease of the N–O stretching band of the parent complex at 1920 cm^{-1} accompanied by an increase of the monocation $\mathbf{[3]}^+$ NO band at 1630 cm^{-1} (Figure 4C). The N–O vibrational frequency of $\mathbf{[3]}^{2+}$ falls well within the range considered for NO^+ state of the ligand, thus implying a 2+ oxidation state of ruthenium.[55,61] On the other hand, a marked 290 cm^{-1} drop of the $\tilde{\upsilon}_{NO}$ upon reduction agrees well with the transformation of the linear Ru^{II}-NO^+ $\{Ru(NO)\}^6$ moiety in $\mathbf{[3]}^{2+}$ to the bent Ru^{II}-NO• $\{Ru(NO)\}^7$ unit in $\mathbf{[3]}^+$, supporting the redox mechanism proposed above.[62] A prolonged reduction of the sample, still in the range of the first electron transfer, resulted in a slow evolution of an additional band at about 1890 cm^{-1}. It is unlikely that this band would correspond to the double reduced Ru^{II}-NO^-, $\{Ru(NO)\}^8$ type, $\mathbf{[3]}^0$ species. A similar behavior was recently reported for a porphyrin complex [Ru(OEP)(NO)Cl].[58]

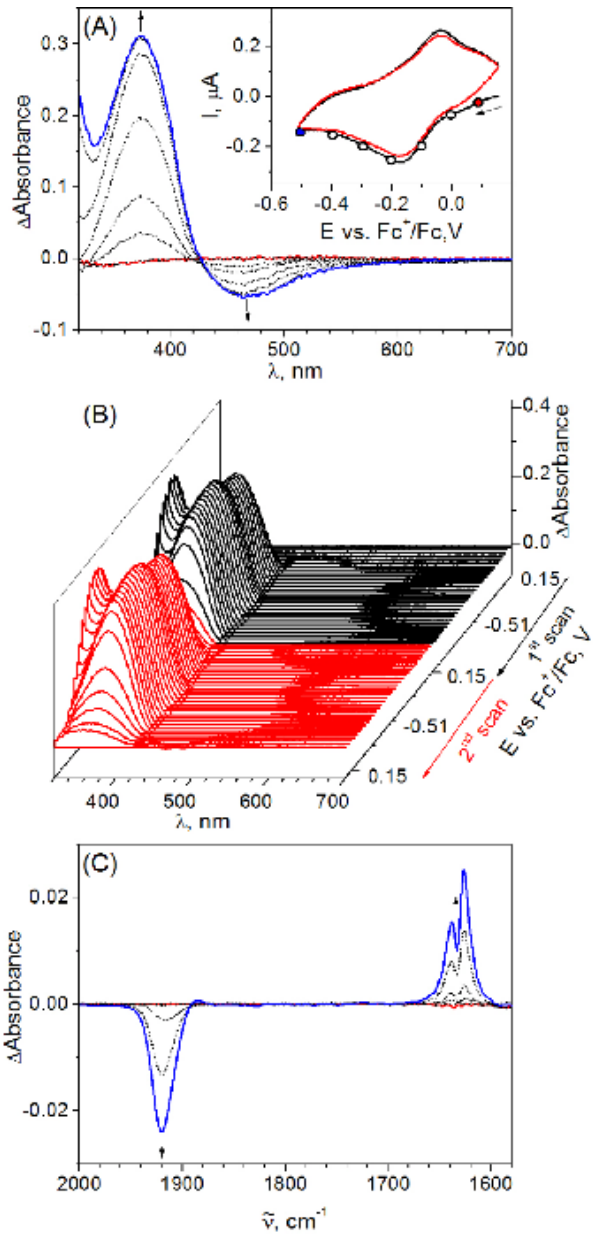

Figure 4. *In situ* UV–vis spectroelectrochemistry for $[\mathbf{3}]^{2+}$ in 0.2 M nBuN$_4$PF$_6$/MeCN (scan rate 10 mV s^{-1}): (A) Difference UV–vis spectra observed upon reduction of $[\mathbf{3}]^{2+}$ going to the first reduction peak. Inset: the corresponding cyclic voltammogram (two consecutive scans) with selected potentials marked with colored circles corresponding to the identically colored optical spectra; (B) Difference UV–vis spectra detected simultaneously upon the reduction of $[\mathbf{3}]^{2+}$ in the region of the first cathodic peak (from +0.15 to –0.51 V vs Fc$^+$/Fc) upon two consecutive cyclic voltammetric scans; (C) *In situ* IR spectroelectrochemistry of $[\mathbf{3}]^{2+}$ in 0.2 M nBuN$_4$PF$_6$/MeCN performed in an OTTLE cell; difference spectra recorded before (red line), upon (dotted lines) and after 30 s reduction at constant potential of –0.5 V vs Fc$^+$/Fc (blue line). The N–O stretching band of the generated $[\mathbf{3}]^+$ at 1630 cm^{-1} overlaps with the scissor vibration band of H_2O in MeCN, thus producing an artifact apparent splitting.

Femtosecond Pump-Probe Spectroscopy. In order to understand the excited state relaxation and NO liberation and recombination dynamics of $[\mathbf{3}]\mathbf{Cl_2}$ and $[\mathbf{4}]\mathbf{Cl_2}$ complexes in solution,

the femtosecond time-resolved transient absorption spectra were measured by exciting at 470 nm in acetonitrile at room temperature. The transient absorption spectra of **[3]Cl_2** at various time delays are shown in Figure 5. At early time scale of 250 fs, a broad transient absorption maximum at around 650 nm is observed. The intensity of the absorption is decreased with increase of delay time and attaining to equilibrium within 30 ps. Similarly transient absorption of **[4]Cl_2** in MeCN were measured (the data is not shown) and signal intensity is weak due to the poor solubility. In order to compare the effect of the trans ligand in the excited state dynamics of the compounds, the kinetic decays of **[3]Cl_2** and **[4]Cl_2** at probing wavelength of 612 nm obtained by exciting at 470 nm are shown in Figure S23. It is observed that the kinetic profiles of both the complexes are similar. The analysis of the femtosecond transient absorption spectra consisting of a three-dimensional data set (wavelength, time, and change in absorbance) was performed with the global analysis program GLOTARAN).[63] Three exponential components, 120 ± 20 fs (τ_1), 570 ± 50 fs (τ_2) and 6.21 ± 0.05 ps (τ_3) were optimally obtained to fully describe the relaxation dynamics of complexes in MeCN.

The excitation of the MLCT band in the ground state absorption spectra using 470 nm generate the highest singlet charge transfer state by transferring the charge from the metal to the ligand and followed by the internal conversion leading to the lowest vibrational state of first singlet state ^{1}MLCT. This leads to the formation of ^{3}MLCT by intersystem crossing. The time constant of these processes could be around or less than the τ_1 which is within the instrumentation limit. The decay of the triplet state (^{3}MLCT) is attributed to the time constants of τ_2. Here it is to be noted that though ^{3}MLCT of $[Ru(bpy)3]^{2+}$ in MeCN solution formed within 100 fs with conversion efficiency of nearly 100% having lifetime of ~ 1 μs,[64] few Ru complexes with short lived or absence of triplet state have been already reported.[65] It is observed that the lifetime of triplet state depends on the Ru–N distance and strength of ligand field.[65a] In addition the contribution of ^{3}LMCT transitions from the unreduced ligand to formerly oxidized Ru(III) center cannot be ruled out.[66] Based on the theoretical studies,[67] it is proposed that the Ru-NO dissociates in the triplet state and the dynamics of NO rebinding occurring with the time constant of τ_3.

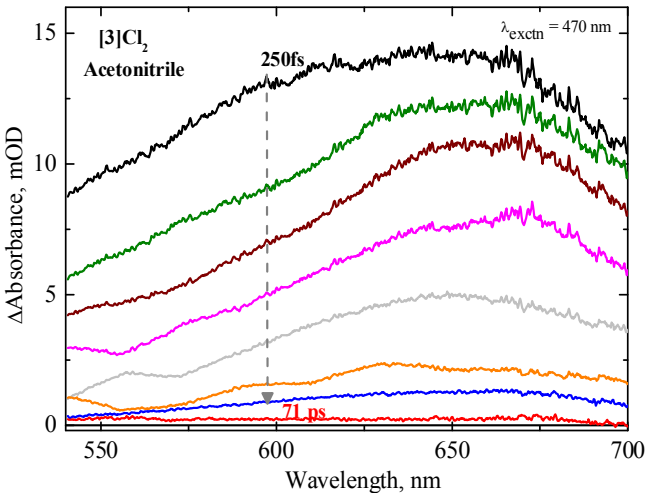

Figure 5. Femtosecond time-resolved transient absorption spectra of **[3]Cl$_2$** in MeCN upon excitation at 470 nm measured at different time delays.

Solution photochemistry in minutes time range. The photochemical behavior of **[3]**$^{2+}$, **[4]**$^{2+}$, **[5]**^{0} and **[6]**^{0} was additionally probed in solution in seconds to minutes time regime. The photo-induced reactivity of a number of {Ru(NO)}^{6} systems at minutes time scale has been previously reviewed,[55] and the typical reaction encountered upon excitation with UV or vis light, is the photo-release of NO$^{\bullet}$ with successive formation of a Ru^{III}-(solv.) complex (equation 1).

$$\{Ru(NO)\}^6 \xrightarrow[solv.]{h\nu} Ru^{III}(solv.) + NO^{\bullet} \qquad (1)$$

We have utilized the specific reaction of NO$^{\bullet}$ with carboxy-2-phenyl-4,4,5,5-tetramethyl-imidazoline-1-oxyl-3-oxide (carboxy-PTIO or cPTIO) nitronyl nitroxide (NN$^{\bullet}$),[68] to follow its expected release upon photolysis of **[3]**$^{2+}$. After the reaction with NO$^{\bullet}$, the NN$^{\bullet}$ transforms to an iminonitroxide (IN$^{\bullet}$), both exhibiting distinct EPR spectra. The solution of **[3]**$^{2+}$ with equimolar amount of cPTIO NN$^{\bullet}$ radical was irradiated in the cavity of the EPR spectrometer with 400 nm LED and the obtained spectra are shown in Figure 6A. The typical quintet signal of the of cPTIO NN$^{\bullet}$ radical (A_{N1} = A_{N3} = 0.76 mT, red line in Figure 6A), gradually transformed to the septet signal of the corresponding IN$^{\bullet}$ (A_{N1} = 0.93 mT, A_{N3} = 0.43 mT, blue line in Figure 6A), confirming thus the NO$^{\bullet}$ photo-release.

The quantification of the NO$^{\bullet}$ photo-release was performed based on the analysis of the UV–vis spectra. The solution of **[3]**$^{2+}$ in MeCN was irradiated with 405 nm light in a LED photoreactor and the *in situ* recorded UV–vis spectra are shown Figure 6B. The irradiation

conditions as well as the sample concentration closely resembled the previous EPR experiment, and since the time scales of the spectral changes observed by both methods correlate, an identical reaction of $NO^{\bullet}$ photo-cleavage was monitored in both cases. The isosbestic points observed in the series of UV–vis spectra (243 nm, 272 nm, Figure 6A) indicate on a clean 1:1 conversion. This was confirmed by the Global Analysis of the obtained data. The first order reaction model according to equation 1, with the rate constant of 6.94×10^{-3} s^{-1} matches well with the spectral changes observed under given experimental conditions. The spectral contribution of the reactant and the product, extracted by the fitting of the kinetic model, are shown in Figure 6C, together with their concentration profiles. Analogously were treated the data from the photolysis experiment in DCM Figure S24C. An axial coordination of a solvent molecule in the photo–generated Ru^{III}(solv) is suggested by eq. 1. Accordingly, the spectrum of the photo-product in DCM shows a different distribution of the intensities of the vis bands, when compared to the photo-product in MeCN. Similar results were also obtained for $\mathbf{[4]^{2+}}$, $\mathbf{[5]^{0}}$ and $\mathbf{[6]^{0}}$ and the spectra are presented in Figures S25–S27.

For the whole series of the ruthenium nitrosyl tetrazole complexes the quantum yields of $NO^{\bullet}$ release obtained for vis irradiation at 405 nm vary between 3–6% and tend to be slightly lower in DCM as compared to the MeCN solutions. These numbers place the investigated compounds into the medium to lower–performing category, among the NO photo-delivering $\{Ru(NO)\}^{6}$ systems.[55] Similar $\Phi_{(NO^{\bullet})}$ was achieved with UVA light, as briefly explored for the $\mathbf{[3]^{2+}}$ (Table 2). The NO liberation efficiency of studied ruthenium nitrosyl tetrazoles is likely limited by the rapid NO rebinding suggested from the investigation of the compound by femtosecond pump-probe spectroscopy. Regarding the influence of the *trans* ligands on the NO photo release efficiency, no apparent correlation is evident at first glance, and a further discussion of the *trans* effect seems to be redundant.

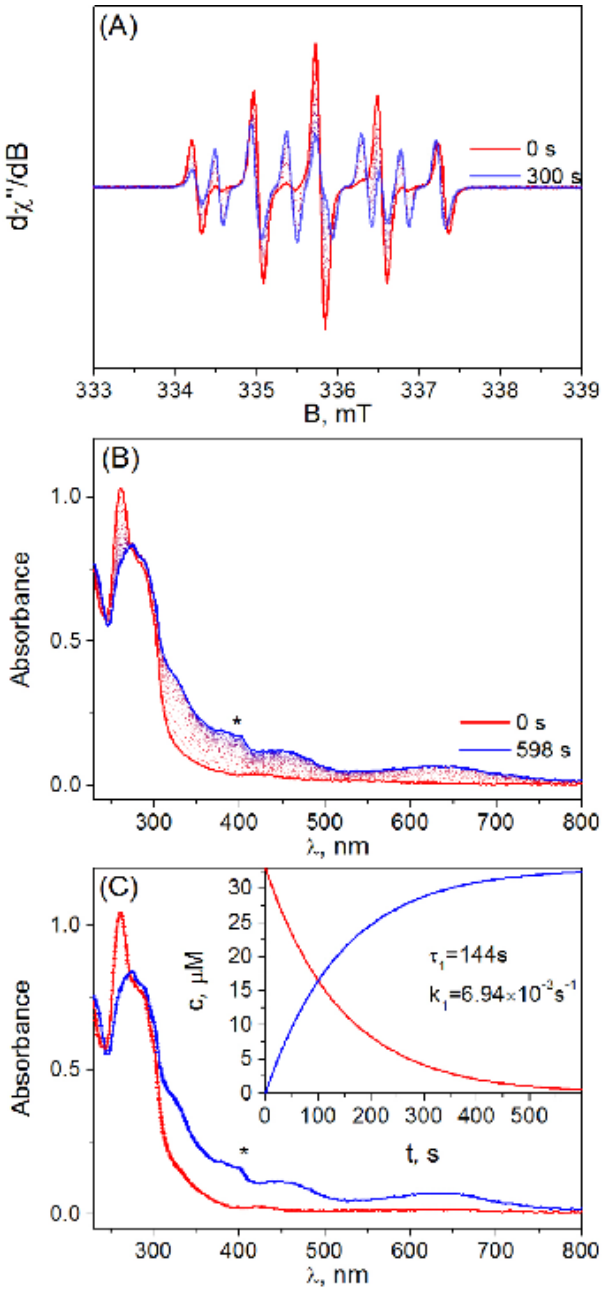

Figure 6. (A) EPR spectra detected upon photolysis (400 nm LED) of 33 μM $\mathbf{[3]^{2+}}$ in the presence of equimolar cPTIO in Ar saturated MeCN. The quintet of cPTIO NN$^{\bullet}$ radical (A_{N1} = A_{N3}= 2.7 MHz or 0.76 mT, red line) transforms to a septet of the corresponding IN$^{\bullet}$ (A_{N1} = 3.3 MHz or 0.93 mT A_{N3}= 1.5 MHz or 0.43 mT, blue line) yielding ~ 60% conversion after 300 s illumination; (B) UV–vis spectra detected *in situ* during photolysis of 33 μM $\mathbf{[3]^{2+}}$ MeCN solution with 405 nm light in a LED photoreactor; (C) The spectra of the $\mathbf{[3]^{2+}}$ (red line) and the photo-product $\mathbf{[3']^{2+(MeCN)}}$ (blue) obtained by the Global Analysis of the spectral series from (B). Inset shows the corresponding concentration-time profiles. * marks an artefact signal.

Table 2. Quantum yields of NO• release.

Complex	Solvent	$\Phi_{(NO•)}$ at 365 nm	$\Phi_{(NO•)}$ at 405 nm
$[\mathbf{3}]^{2+}$	MeCN	0.038±0.006	0.045±0.005
	DCM	–	0.033±0.006
$[\mathbf{4}]^{2+}$	MeCN	–	0.040±0.005
	DCM	–	0.034±0.006
$[\mathbf{5}]^{0}$	MeCN	–	0.038±0.003
	DCM	–	0.032±0.004
$[\mathbf{6}]^{0}$	MeCN	–	0.062±0.005
	DCM	–	0.032±0.004

DFT Calculations. The optimized geometries of the initial $[\mathbf{3}]^{2+}$, $[\mathbf{4}]^{2+}$ and $[\mathbf{5}]^{0}$ (singlet states) complexes agree well with the found crystal structures (see Table S3). The additional modes of NO binding to Ru, documented in the literature (T-shape and {Ru-ON}) [43,44,45,46,47,69,70] are energetically not favored (see Table S4). Nevertheless, the calculated NO vibration of T-shape geometry $[\mathbf{3}]^{2+(T)}$ (ν_{NO} = 1743 cm^{-1}) and the experimentally obtained band found at 1630 cm^{-1} (Figure 4C) are in a qualitative agreement. The situation is the same for the other relevant structures (see Table S4).

The reduced system $[\mathbf{3}]^{+}$ (doublet state) has a bent structure[71] (with Ru–N3–O1 angle around 140°) due to the antibonding Ru-(NO) π*-character of closely degenerate LUMO/LUMO+1 (see Figure S29). In addition, this geometry of the $[\mathbf{3}]^{+}$ is further stabilized by O1···H–N_{ind} hydrogen bond. Most of the spin density of $[\mathbf{3}]^{+}$ (*ca*. 77 %) is localized on the NO group, while *ca*. 17% of spin is on the Ru atom, see Figure 7A.

After the release of NO radical (NO•) from $[\mathbf{3}]^{2+}$, the unpaired electron of the $^{2}[RuCl(Hind)_4]^{2+}$ residue (from hereafter labeled as $[\mathbf{3'}]^{2+}$) is with ca. 74% of spin density localized on Ru (in the non-bonding $4d_{xy}$ orbital), see Figure 7B. This holds also for the $[\mathbf{3'}]^{2+(MeCN)}$ species (where the released NO• is replaced by MeCN solvent molecule), see Figure S30B. The formal electronic structure of Ru^{III} atom in $[\mathbf{3'}]^{2+}$is $[Kr^{54}]4d_{xz}^{2}4d_{yz}^{2}4d_{xy}^{1}$. The formal single reference electron configuration of {Ru-NO}^{6} moiety when taking into account the 5d electrons of Ru^{III} and the unpaired electron of NO in $[\mathbf{3}]^{2+}$ is $[Kr^{54}]4\pi_x^{2}4\pi_y^{2}4d_{xy}^{2}$. The d-populations (physical electronic configuration/structure) of Ru in $[\mathbf{3}]^{+}$, $[\mathbf{3}]^{2+}$ and $[\mathbf{3'}]^{2+}$ are $[Kr^{54}]4d_{xz}^{1.75}4d_{yz}^{1.52}4d_{xy}^{1.89}$, $[Kr^{54}]4d_{xz}^{1.45}4d_{yz}^{1.45}4d_{xy}^{1.94}$ and $[Kr^{54}]4d_{xz}^{1.91}4d_{yz}^{1.91}4d_{xy}^{1.27}$, respectively. Hence, one can see the significant change of the electronic configuration of Ru upon the NO• release.

TD-DFT level of theory was used to qualitatively interpret the experimental vis absorption spectrum of **[3]**$^{2+}$. One can assign the most prominent excitations to transitions from the frontier orbitals of Hind character (HOMO–3 - HOMO) into the unoccupied π* (LUMO and LUMO+1, see Figure S29) and σ* (LUMO+2, see Figure S29) Ru–NO antibonding orbitals, where the π* transitions have been previously identified in a similar {Ru(NO)}^{6} system.[67] The transitions into π* Ru–NO antibonding orbital are red shifted (500–650 nm), whereas the transitions to σ* Ru–NO antibonding orbitals are blue shifted (400 nm). (The visualization of the difference densities and relaxed densities is shown in Figure S31.) The π* and σ* Ru–NO excitations are the initial channels of the Ru–NO dissociation pathway upon photolysis.

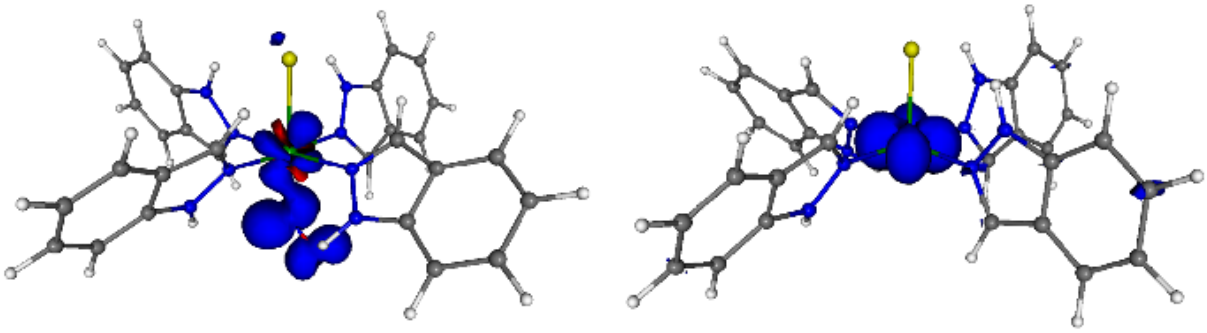

(A) (B)

Figure 7. B3LYP/SVP(SDD) spin densities of **[3]**$^{+(1)}$ lower in energy (A) and of **[3']**$^{2+}$ (B), isovalue ±0.005.

The collective ^{1}H NMR, ESI MS and UV–vis solution equilibrium studies revealed that **[3]Cl$_2$** and **[4]Cl$_2$** are compatible with aqueous media. There were no major changes of the UV–vis spectra of **[3]Cl$_2$** upon pH variation from 2 to ca 11 in 50% ethanol/water solution attesting that there was no conversion to other species (e.g., via aquation, decomposition, etc.). For **[4]Cl$_2$** protonation of OH^- at more acidic conditions is envisaged, and the involvement of Hind ligands into a pH dependent process, namely, deprotonation, without liberation of indazole proligands, as evidenced by ^{1}H NMR and spectrofluorimetric measurements. These investigations along with the ability of the compounds to release NO in solution upon excitation encouraged us to further investigate their biological potential.

The collective ^{1}H NMR, ESI MS and UV–vis solution equilibrium studies revealed that **[3]Cl$_2$** and **[4]Cl$_2$** are compatible with aqueous media. There were no major changes of the UV–vis spectra of **[3]Cl$_2$** upon pH variation from 2 to ca 11 in 50% ethanol/water solution attesting that there was no conversion to other species (no ligand-exchange took place). For **[4]Cl$_2$** protonation of OH^- at more acidic conditions is envisaged, and the involvement of

Hind ligands into a pH dependent process, namely, deprotonation, without liberation of indazole proligands, as evidenced by ^{1}H NMR and spectrofluorimetric measurements. These investigations along with the ability of the compounds to release NO in solution upon excitation encouraged us to further investigate their biological potential.

Antiproliferative activity in cancer cell lines. The antiproliferative effects of complexes **1, [3]Cl$_2$**, and **[4]Cl$_2$** in comparison with cisplatin were determined by colorimetric cell viability assay (MTT assay) against a panel of cancer cell lines. The IC_{50} values are quoted in Table 4 and the concentration-effect curves are shown in Figure S32.

Table 4. Cytotoxicities of complexes **[1]**, **[3]Cl$_2$**, **[4]Cl$_2$**, **cisplatin and KP1019**

Compound	IC_{50} [a] [μM]			
	HCT116	A2780	HEK293	SF
[1]	1.1 ± 0.2	0.25 ± 0.04	0.53 ± 0.03	2.1
[3]Cl$_2$	0.65 ± 0.19	0.33 ± 0.02	0.61 ± 0.10	1.8
[4]Cl$_2$	1.1 ± 0.5	0.23 ± 0.03	1.2 ± 0.2	5.2
Cisplatin	0.86 ± 0.16	0.60 ± 0.05	3.8 ± 1.3	6.3
KP1019	31 ± 8	16 ± 2	29 ± 5	1.8

[a] 50% inhibitory concentrations in human colorectal carcinoma cells HCT116, human ovarian carcinoma cell lines A2780 and non-cancerous HEK293 cells, determined by MTT assay. Values are means plus/minus standard deviations obtained from at least three independent experiments with exposure times of 72h. Selectivity Factor (SF) is determined as $IC_{50\ (HEK293)}/IC_{50\ (A2780)}$.

In general, all tested complexes demonstrated high antiproliferative activity in sub-micromolar or low micromolar concentration range in cancerous cell lines and no significant differences between the cytotoxicity of complexes **[1]**, **[3]Cl$_2$** and **[4]Cl$_2$** were observed. The antiproliferative activity of complex **[1]** in CH1 and SW480 after 96 h exposure has been previously reported[16] and the IC_{50} values were comparable to those obtained in the present work. Mono-indazole ruthenium-nitrosyl complexes, which bear some structural resemblance to complexes **[3]Cl$_2$** and **[4]Cl$_2$**, were tested in CH1/PA-1, SW480 and A549 cells after 96 h exposure and also demonstrated antiproliferative activity in a micromolar concentration range.[15] Importantly, the complexes displayed higher activity than KP1019 and cisplatin in all tested cell lines. Next, we tested the selectivity of complexes **[1]**, **[3]Cl$_2$** and **[4]Cl$_2$** towards cancer cells vs healthy cells. Based on our results, all complexes showed some degree of selectivity towards embryonic kidney cells HEK293 cells over A2780 cells, but lower than

that of cisplatin. Surprised by these results, we additionally determined the selectivity factor for KP1019, which is known to demonstrate uniquely low toxicity in cancer patients in comparison with highly toxic cisplatin.[72,73,74] As can be seen from Table 5, the selectivity of KP1019 towards cancer cells over healthy cells was lower than that of cisplatin. Therefore, even though HEK293 cells are very commonly used for the assessment of toxicity in non-cancerous cell lines, the results should be treated with caution.

The role of NO ligand in the anticancer activity. In order to determine the effects of NO ligand on the cytotoxicity of Ru nitrosyl complexes, we assessed the antiproliferative activity of complexes **[3]Cl$_2$** and **[4]Cl$_2$** in presence of cPTIO as NO$^\bullet$ scavenger (*vide supra*).[68] cPTIO is also used to determine if NO$^\bullet$ plays a role in various biological processes, such as DNA fragmentation,[75,**Hiba! A könyvjelző nem létezik.**] platelet aggregation,[76] endotoxin shock[77] and cytotoxic effects.[78] In order to choose the appropriate concentration of cPTIO for subsequent experiments with Ru-NO complexes, its cytotoxicity was determined by MTT assay in A2780 cells with exposure time of 72 h. Subsequently, complexes **[3]Cl$_2$** and **[4]Cl$_2$** were co-incubated with 2.5 and 10 μM of carboxy-PTIO for 72 h and their cytotoxicity was determined by MTT assay. Based on the results of MTT (Figure S32), the cytotoxicity of complexes **[3]Cl$_2$** and **[4]Cl$_2$** was not inhibited in the presence of cPTIO. Subsequently, complexes **[3]Cl$_2$** and **[4]Cl$_2$** were irradiated by blue LED light (max emission at around 470 nm) for 5 min and their cytotoxicity was compared to the activity of these complexes without irradiation. To mimic the conditions of NO photo-release experiments, **[3]Cl$_2$** and **[4]Cl$_2$** were dissolved in MeCN and it was ensured that the cell viability was not affected by the presence of organic solvent. As can be seen in Figure S33, the cytotoxicity of complexes **[3]Cl$_2$** and **[4]Cl$_2$** upon irradiation increased by ca. 30%. Subsequently, the activity of the complexes upon irradiation was evaluated in the presence of carboxy-PTIO and no changes in cytotoxicity were detected. Therefore, based on the results of the MTT experiments, the role of NO ligand in the cytotoxicity of **[3]Cl$_2$** and **[4]Cl$_2$** was not confirmed.

p53 Dependence. The majority of clinically used anticancer compounds exhibit their mode of action by activating p53 pathway in cancer cells. p53 protein plays the key role in determining cell fate and in case if the damage is too excessive, p53 triggers cell death.[79,80] However, most of cancer cells are able to cause p53 mutations leading to the loss of its protective function and resistance to common chemotherapies. Hence, the very design of the traditional

anticancer treatment is often defeated by cancer cells properties and the identification of p53-independent compounds is highly desirable. In order to assess the role of p53 protein in the antiproliferative activity of ruthenium complexes, we determined the cytotoxicity of compounds in HCT116 colorectal cancer cell line and its resistant analogue HCT116 p53 $^{-/-}$, where p53 gene was knocked out (Table 5).

Table 5. Cytotoxicities of complexes **1**, **[3]Cl$_2$**, **[4]Cl$_2$**, **cisplatin** and **oxaliplatin**

Compound	IC_{50} [a] [μM]				
	HCT116 wt	HCT116 wt + pifithrin α	Ratio IC_{50} with/without inhibition	HCT116 $p53^{-/-}$	Ratio IC_{50} $p53^{-/-}$ /wt
[1]	1.1 ± 0.2	1.1 ± 0.3	1.0	1.5 ± 0.2	1.5
[3]Cl$_2$	0.65 ± 0.19	0.52 ± 0.11	0.8	0.66 ± 0.15	1.0
[4]Cl$_2$	1.1 ± 0.5	1.4 ± 0.3	1.3	0.9 ± 0.2	0.8
Cisplatin	5.2 ± 1.3	9.0 ± 1.2	1.7	12 ± 2	2.3
Oxaliplatin	0.86 ± 0.16	1.9 ± 0.4	2.2	4.1 ± 0.9	4.8

[a] 50% inhibitory concentrations in colorectal carcinoma cells HCT116wt (wild type) and HCT116 $p53^{-/-}$ determined by MTT assay. Values are means plus/minus standard deviations obtained from at least three independent experiments with exposure times of 72h.

The results were compared to cisplatin and oxaliplatin, which are known to be p53-dependent. As expected, both cisplatin and oxaliplatin demonstrated strong dependence on p53 and their activity in p53-null cell line was 2–5 times lower than in the parental HCT116 cell line. On the contrary, all ruthenium complexes were equally potent in both HCT116 cell lines, indicating their independence from p53. To further confirm the observed effects, the cytotoxicity of compounds was tested in the presence of p53 inhibitor, pifithrin α. Pifithrin α is known to inhibit both p53-mediated apoptosis and p53-mediated gene transcription such as cyclin G1 and p21/waf1 expression.[81,82] In agreement with the results of MTT assay in isogenic HCT116 cell lines, the activity of cisplatin and oxaliplatin was suppressed by p53 inhibition albeit to a lesser extent than by p53 gene knock out, whereas ruthenium complexes were not affected by pifithrin α. Additionally, the effects of metal complexes on p53 protein expression were evaluated by Western Blot in A2780 cells (Figure 17). As expected, cisplatin and oxaliplatin caused significant overexpression of p53, whereas ruthenium complexes did not have any effect on p53 expression. Therefore, it can be concluded that p53-independent mode of action of ruthenium complexes is retained in various cell lines. It should be noted

that other ruthenium compounds were also shown to be independent from p53 cellular status.[71,83,84]

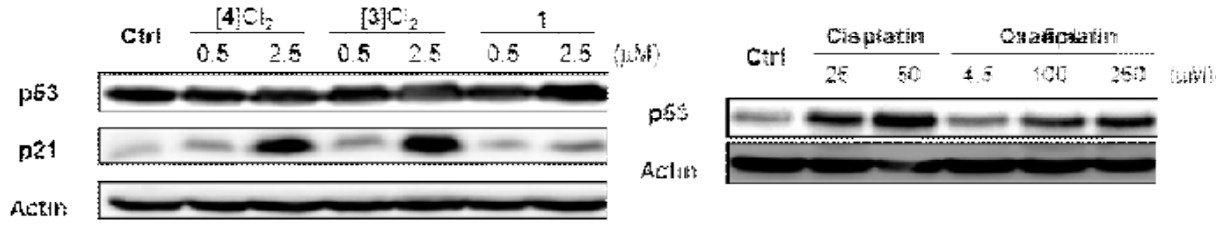

Figure 17. Western blot analysis of p53 and p21 proteins. A2780 cells were collected after incubation with compounds of interest at indicated concentrations for 24 h. Total lysates were isolated and examined by western blot. Actin was used as a loading control.

When the cell's DNA is damaged, various cell mechanisms are activated in order to repair the damage or trigger the cell to systematically kill itself. As it was mentioned previously, the key role in determining cell fate is played by p53 protein; however, the decision whether cells live or die is also dependent on p53 downstream effector p21. The cyclin-dependent kinase (cdk) inhibitor p21 plays an important role in genomic stability, apoptosis, senescence and DNA repair.[85] It is also known that it can be activated in a p53-dependent and independent manner. To understand if the observed antiproliferative effects of ruthenium complexes **[1]**, **[3]Cl$_2$** and **[4]Cl$_2$** were related to the induction of overexpression of p21, we performed western blot analysis of p21 marker. Incubation of cells with complexes of interest at various concentrations for 24 h caused a dose-dependent increase in the magnitude of induction of p21 protein. The regulation of p21 might be the cause of antiproliferative action of novel ruthenium complexes.

Conclusions

By reaction of *trans*-[Ru(NO$_2$)$_2$(Hind)$_4$] (**[2]**) with 12M and 3M hydrochloric acid in methanol new complexes *trans*-[RuCl(Hind)$_4$(NO)]Cl$_2$·H$_2$O (**[3]Cl$_2$·H$_2$O**) and *trans*-[RuOH(Hind)$_4$(NO)]Cl$_2$·H$_2$O (**[4]Cl$_2$·H$_2$O**), respectively, were synthesized in good yields. Deprotonation at pH 6–9 led to isolation of two other compounds, namely [RuCl(ind)$_2$(Hind)$_2$(NO)] (**[5]**) and [RuOH(ind)$_2$(Hind)$_2$(NO)] (**[6]**), respectively. These results might also shed light on the nature of the green species generated from KP1019 at physiological pH, which posed a problem upon intravenous administration in cancer patients.

Upon light irradiation solid **[3]Cl_2·H_2O** did not exhibit significant metastable isomer population, but considerable NO release at room temperature. In contrast, for **[4]Cl_2·H_2O** and **[5]** we observed both phenomena NO release at room temperature and reversible linkage isomerism at low temperature.

[3]Cl_2 was found to be redox active in MeCN undergoing one reversible one-electron reduction confirmed by coulometric measurements at $E_{1/2}$ = –0.11 V followed by a second quasireversible one-electron reduction at $E_{1/2}$ = –0.80 V vs Fc^+/Fc. Both reductions are predominantly NO centered as was also confirmed by IR-spectroelectrochemistry, X- and Q-band EPR spectroscopy and DFT calculations. In particular, the first reduction step is accompanied by a decrease of NO stretching band at 1920 cm^{-1} and appearance and increase of a new NO band at 1630 cm^{-1}. This drop of $\tilde{\upsilon}_{NO}$ is due to bending of linear Ru^{II}-NO^+ moiety into Ru^{II}-NO• (calcd Ru–N–O 141.29°).

The photo-induced release of NO upon irradiation of **[3]Cl_2** and **[4]Cl_2** in solution with 400 nm LED has been confirmed by EPR spectroscopy by monitoring the specific reaction of $NO^•$ with nitronyl nitroxide ($NN^•$) to give iminonitroxide ($IN^•$). The quantification of the NO release performed by analysis of the UV–vis spectra indicates 3–6% based on calculated quantum yields at 405 nm (Table 3). These numbers are quite reasonable given the low excitation coefficients at 405 nm (ca. 500 $M^{-1}cm^{-1}$) and are in accord with femtosecond pump probe spectroscopy data, which indicated almost cyclic liberation and rebinding of NO to ruthenium upon excitation. To increase the biological utility of this type of compounds we are going to explore one of the strategies proposed previously for photosensitizing the Ru–NO bond to visible light,[55] namely by modifying the azole heterocycles in order to increase their electron donating ability. In particular, replacement of 1*H*-indazole ligands by 3,5-dimethyl-1*H*-pyrazole is envisaged.

The complexes **[3]Cl_2·H_2O** and **[4]Cl_2·H_2O** show high antiproliferative activity, which is p53 independent. However, the compounds caused overexpression of p21 and the regulation of its status might be the reason of activity at the molecular level. Release of NO, if any, does not contribute significantly to antiproliferative activity.

ASSOCIATED CONTENT

Supporting Information

ORTEP view of **[2]** (Figure S1), IR spectra measured under light irradiation (Figures S2–S4), UV–vis spectra, ^{1}H NMR spectra, and fluorescence emission spectra of **[3]Cl$_2$** and **[4]Cl$_2$** under different conditions (Figures S5–S8), cyclic voltammetry of new complexes (Figures S9–S11), EPR spectra (Figures S12–S20), UV–vis spectra of **[3]**$^{2+}$ and **[3]**$^{+}$ (Figure S21), UV–vis spectra of **[4]**$^{2+}$ detected simultaneously upon reduction (Figure S22), kinetic data from femtosecond transient absorption spectra of **[3]Cl$_2$** and **[4]Cl$_2$** (Figure S23), UV–vis spectra of complexes detected in situ during photolysis (Figures S24–S27), TDDFT calculated UV–vis spectra (Figure S28), other results of DFT calculations (Figures S29–S31, Tables S2–S4), concentration-effect curves from MTT assays and IC_{50} values without and with illumination (Figures S32 and S33), crystal data and details of data collection (Table S1).

AUTHOR INFORMATION

Corresponding Author

*E-mail: vladimir.arion@univie.ac.at (V. B. Arion)

ORCID

Peter Rapta: 0000-0001-6071-3932

Michal Zalibera: 0000-0002-6527-1982

Maria Babak: 0000-0002-2009-7837

Wee Han Ang: 0000-0003-2027-356X

Vladimir B. Arion: 0000-0002-1895-6460

Notes

The authors declare no competing financial interest.

ACKNOWLEDGMENTS

We thank MSc Laura Alice Hager for her help in the synthesis of **[3]Cl$_2$** and **[4]Cl$_2$**, Alexander Roller for X-ray diffraction measurements and Jozef Zlámal for photolysis experiments. We acknowledge the financial support of the Slovak Research and Development Agency (APVV-15-0053, APVV-15-0079), Slovak Scientific Grant Agency VEGA (1/0416/17, 1/0466/18, 1/0871/16, 1/0598/16) and the Ministry of Education, Science, Research and Sport of the Slovak Republic Excellent research teams program. MM is also grateful to Fundação para a Ciência e a Tecnologia (FCT/MEC) and FEDER funds under the Partnership Agreement PT2020, through projects UID/QUI/50006/2013, POCI/01/0145/FEDER/007265, and NORTE-01-0145-FEDER-000011 (LAQV@REQUIMTE). We are grateful to the HPC center at the Slovak University of Technology in Bratislava, which is a part of the Slovak Infrastructure of High Performance Computing (SIVVP project, ITMS code 26230120002, funded by the European Regional Development Funds), for the computational time and resources made available. This work was also supported by the National Research, Development and Innovation Office FK 124240 and GINOP-2.3.2-15-2016-00038 projects.

References

1. Ozkon, V. S.; Agarwal, U. S.; Marcelin, S. W. (Eds.), Reduction of Nitrogen Oxide Emissions; ACS Symposium Series 587, American Chemical Society, Washington, DC, 1995.

2. Koshland, Jr., D. E. The molecule of the year, *Science* **1992**, *258*, 1861.

3. McCleverty, J. A. Chemistry of nitric oxide relevant to biology, *Chem. Rev.* **2004**, *104*, 403–418.

4. Lagadec, P.; Raynal, S.; Lieubeau, B.; Onier, N.; Arnould, L.; Saint-Giorgio, V.; Lawrence, D. A.; Jeannin, J.-F. Evidence for control of nitric oxide synthesis by intracellular transforming growth factor-β1 in tumor cells. *Am. J. Pathol.* **1999**, *154*, 1867–1876.

5. Hickok, J. R.; Thomas, D. D. Nitric oxide and cancer therapy: the Emperor has NO clothes. *Curr. Pharm. Des*. **2010**, *16*, 381–391.

6. Serli, B.; Zangrando, E.; Iengo, E.; Mestroni, G.; Yellowlees, L.; Alessio, E. Synthesis and structural, spectroscopic, and electrochemical characterization of new ruthenium dimethyl sulfoxide nitrosyls. *Inorg. Chem.* **2002**, *41*, 4033–4043.

7. Serli, B.; Zangrando, E.; Gianferrara, T.; Yellowlees, L.; Alessio, E. Coordination and release of NO by ruthenium-dimethylsulfoxide complexes – implications for metastases activity. *Coord. Chem. Rev.* **2003**, *245*, 73–83.

8. Thomas, D. D.; Espey, M. G.; Ridnour, L. A.; Hofseth, L. J.; Mancardi, D.; Harris, C. C.; Wink, D. A. Hipoxic inducible factor 1α, extracellular signal-regulated kinase, and p53 are regulated by distinct threshold concentrations of nitric oxide. *Proc. Natl. Acad. Sci. USA* **2004**, *101*, 8894–8899.

9. Thomas, D. D.; Miranda, K. M.; Espey, M. G.; Citrin, D.; Jourd'heuil, D.; Paolocci, N.; Hewett, S. J.; Colton, C. A.; Grisham, M. B.; Feelissch, M.; Wink, D. A. Guide for the use on nitric oxide (NO) donors as probes of the chemistry of NO and related redox species in biological systems. *Methods Enzymol*. **2002**, *359*, 84–105.

10. Lahiri, G. K.; Kaim, W. Electronic structure alternatives in nitrosylruthenium complexes. *Dalton Trans.* **2010**, *39*, 4471–4478.

11. Coe, B. J.; Glenwright, S. J. Trans-effects in octahedral complexes. *Coord. Chem. Rev.* **2000**, *203*, 5–80.

12. (a) Zanichelli, P. G.; Estrela, H. F. G.; Spadari-Bratfisch, R. C.; Grassi-Kassisse, D. M.; Franco, D. W. The effects of ruthenium tetraammine compounds on vascular smooth muscle.

Nitric Oxide: Biol. Chem. 2007, *16*, 189–196; (b) de Candia, A. G.; Singh, P.; Kaim, W.; Slep, L. D. All-*trans*-[$ClRu^{II}(py)_4(NC)Ru^{II}(py)_4(CN)Ru^{II}(py)_4(NO)][PF_6]_4$: a redox-active 2-donor/1-acceptor system based on the electrophilic $\{RuNO\}^6$ motif. *Inorg. Chem.* 2009, *48*, 565–573.

13. (a) Tfouni, E.; Krieger, M.; McGarvey, B. R.; Franco, D. W. Structure, chemical and photochemical reactivity and biological activity of some ruthenium amine nitrosyl complexes. *Coord. Chem. Rev.* **2003**, *236*, 57–69; (b) Bordini, J.; Novaes, D. O.; Borissevitch, I. E.; Owens, B. T.; Ford, P. C.; Tfouni, E. Acidity and photolability of ruthenium salen nitrosyl and aquo complexes in aqueous solution. *Inorg. Chim. Acta* **2008**, *361*, 2252–2258.

14. Rathgeb, A.; Böhm, A.; Novak, M. S.; Gavriluta, A.; Dömötör, O.; Tommasino, J. B.; Enyedy, É. A.; Shova, S.; Meier, S.; Jakupec, M. A.; Luneau, D.; Arion, V. B. Ruthenium-nitrosyl complexes with glycine, L-alanine, L-valine, L-proline, L-serine, L-threonine, and L-tyrosine: synthesis, X-ray diffraction structures, spectroscopic and electrochemical properties, and antiproliferative activity. *Inorg. Chem*. **2014**, *53*, 2718−2729.

15. Büchel, G. E.; Gavriluta, A.; Novak, M.; Meier, S. M.; Jakupec, M. A.; Cuzan, O.; Turta, C.; Tommasino, J.-B.; Jeanneau, E.; Novitchi, G.; Luneau, D.; Arion, V. B. Striking difference in antiproliferative activity of ruthenium- and osmium-nitrosyl complexes with azole heterocycles. *Inorg. Chem.* **2013**, *52*, 6273–6285.

16. Jakupec, M. A.; Reisner, E.; Eichinger, A.; Pongratz, M.; Arion, V. B.; Galanski, M.; Hartinger, C. G.; Keppler, B. K. Redox-active antineoplastic ruthenium complexes with indazole: correlation of in vitro potency and reduction potential. *J. Med. Chem.* **2005**, *48*, 2831–2837.

17. Irving, H. M.; Miles, M. G; Pettit, L. D. A study of some problems in determining the stoicheiometric proton dissociation constants of complexes by potentiometric titrations using a glass electrode. *Anal. Chim. Acta* **1967,** *38*, 475–488.

18. Stoll, S.; Schweiger, A.; EasySpin, a comprehensive software package for spectral simulation and analysis in EPR. *J. Magn. Reson.* **2006**, *178*, 42–55.

19. Kuhn, H.; Braslavsky, S.; Schmidt, R.;. Chemical actinometry (IUPAC Technical Report). *Pure Appl. Chem.* **2009,** *76*, 2105–2146.

20. van Wilderen, L.J.G.; Lincoln, C.N.; van Thor, J.J.; Modelling Multi-Pulse Population Dynamics from Ultrafast Spectroscopy. *PLoS ONE* **2011**, *6*, e17373.

21. Karunakaran, V.; Das, S. Direct observation of cascade of photoinduced ultrafast intramolecular charge transfer dynamics in diphenyl acetylene derivatives: via solvation and intramolecular relaxation. *J. Phys. Chem. B*. **2016**, 120, 7016–7023.
22. Becke, A. D. Density-functional exchange-energy approximation with correct asymptotic behavior. *Phys. Rev. A* **1988**, *38*, 3098–3100.
23. Lee, C.; Yang, W.; Parr, R. G. Development of the Colic-Salvetti Correlation-Energy Formula into a Functional of the Electron D. *Phys. Rev. B* **1988**, *37*, 785–789.
24. Becke, A. D. Density-functional thermochemistry.III. The role of exact exchange. *J. Chem. Phys.* **1993**, *98*, 5648.
25. Vosko, S. H.;Wilk, L.; Nusair, M. Accurate spin-dependent electron liquid correlation energies for local spin density calculations: a critical analysis. *Can. J. Phys.* **1980**, *58*, 1200–1211.
26. Weigand, F.; Ahlrichs, R. Balanced basis sets of split valence, triple zeta valence and quadruple zeta valence quality for H to Rn: Design and assessment of accuracy. *Phys. Chem. Chem. Phys.* **2005**, *7*, 3297–3305.
27. Andrae, D.; Häusserman, U.; Dolg, M.; Stoll, H.; Preus, H.W. Energy-adjusted ab initio pseudopotentials for the second and third row transition elements. *Theor. Chim. Acta* **1990**, *77*, 123–141.
28. Frisch, M. J. et al. Gaussian, Inc., Wallingford CT, **2009.** Gaussian Inc. Wallingford CT 2009.
29. Dyall, K. G. Relativistic double-zeta, triple-zeta, and quadruple-zeta basis sets for the 6d elements Rf-Cn. *Theor. Chem. Acc.* **2011**, *129*, 603–613.
30. Neese, F. The ORCA program system. In *Wiley Interdisciplinary Reviews: Computational Molecular Science* **2012**, *2*, 73–78.
31. Neese, F. Metal and Ligand Hyperfine Couplings in Transition Metal Complexes. The Effect of Spin-Orbit Coupling as Studied by Coupled Perturbed Kohn-Sham Theory. *J. Chem. Phys.* **2003**, *118*, 3939–3948.
32. Neese, F. Efficient and accurate approximations to the molecular spin-orbit coupling operator and their use in molecular g-tensor calculations. *J. Chem. Phys.* **2005**, *122*, 34107.
33. Douglas, M.; Kroll, N.M. Quantum Electrodynamical Corrections to Fine-Structure of Helium. *Ann. Phys.* **1974**, *82*, 89.

34. Hess, B.A. Applicability of the no-pair equation with free-particle projection operators to atomic and molecular structure calculations. *Phys. Rev. A* **1985**, *32*, 756–764.
35. Wolf, A.; Reiher, M.; Hess, B.A. The generalized Douglas-Kroll transformation. *J. Chem. Phys.* **2002**, *117*, 9215–9226.
36. Neese, F.; Wolf, A.; Fleig, T.; Reiher, M.; Hess, B. A. Calculation of electric-field gradients based on higher-order generalized Douglas-Kroll transformations. *J. Chem. Phys.* **2005**, *122*, 1–10.
37. Wolf, A.; Reiher, M. Exact decoupling of the Dirac Hamiltonian. III. Molecular properties. *J. Chem. Phys.* **2006**, *124*, 1–11.
38. Flükiger, P.; Lüthi, H. P.; Sortmann, S.; Weber, J. Molekel 4.3, Swiss Center for Scientific Computing, Manno (Schweiz), 2000–2002.
39. Fackler, J. P., Jr.; Staples, R. J.; Raptis, R. G. Crystal structure of cis-bis(triphenylphosphine)platinum(II)-chloro-N-indazolate, $PtCl[P(C_6H_5)_3]_2(C_7H_5N_2)$. *Z. Kristallogr.* **1997**, *212*, 157–158.
40. Schuecker, R.; John, R. O.; Jakupec, M. A.; Arion, V. B.; Keppler, B. K. Water-soluble mixed-ligand ruthenium(II) and osmum(II) arene complexes with high antiproliferative activity. *Organometallics* **2008**, *27*, 6587–6595.
41. Hauser, U.; Oestreich, V.; Rohrweck, H. D. On optical dispersion in transparent molecular systems. I. Mössbauer resonance observation of a new kind of isomeric molecular states generated by polarized light. *Z. Phys. A* **1977**, *280*, 17–25.
42. Hauser, U.; Oestreich, V.; Rohrweck, H. D. On optical dispersion in transparent molecular systems. II. Properties of the new kind of isomeric molecular states generated by coherent light. *Z. Phys. A* **1977**, *280*, 125–130.
43. Woike, T.; Zöllner, H.; Krasser, W.; Haussühl, S. Raman-spectroscopic and differential scanning calorimetric studies of the light induced metastable states in $K_2[RuCl_5NO]$. *Solid State Commun.* **1990**, *73*, 149–152.
44. Woike, T.; Haussühl, S. Infrared-spectroscopic and differential scanning calorimetric studies of the light induced metastable states in $K_2[Ru(NO_2)_4(OH)NO]$. *Solid State Commun.* **1993**, *86*, 333–337.
45. P. Coppens, I. Novozhila, A. Kovalevsky, Photoinduced linkage isomers of transition-metal mitrosyl compounds and related complexes. *Chem. Rev.* **2002**, *102*, 861–883.

46. D. Schaniel, T. Woike, B. Delley, C. Boskovic, D. Biner, K. W. Krämer, H. U. Güdel, Long-lived light-induced metastable states in *trans*-$[Ru(NH_3)_4(H_2O)NO]Cl_3 \cdot H_2O$. *Phys. Chem. Chem. Phys.* **2005**, *7*, 1164–1170.

47. D. Schaniel, B. Cormary, I. Malfant, L. Valade, T. Woike, B. Delley, K. W. Krämer, H. U. Güdel, Photogeneration of two metastable NO linkage isomers with high populations of up to 76% in *trans*-$[RuCl(py)_4(NO)][PF_6]_2 \cdot ½H_2O$. *Phys. Chem. Chem. Phys.* **2007**, *9*, 3717–3724.

48. Kobayashi, H. Cancer chemotherapy specific to acidic nests. *Cancers* **2017**, *9*, 36; doi:10.3390/cancers9040036.

49. (a) Wike-Hooley, J. L.; Haveman, J.; Reinhold, H. S. The relevance of tumour pH to the treatment of malignant disease. *Radiother. Oncol*. **1984**, *2*, 343–366; (b) Ashby, B. S.; Cantab, M. B. pH-Studies in human malignant tumours. *Lancet* 1966, 2, 312–315.

50. Pieper, T.; Peti, W.; Keppler B. K. Solvolysis of the tumor-inhibitting Ru(III)-complex trans-tetrachlorobis(indazole)ruthenate(III). *Metal-Based Drugs* **2000**, *7*, 225–232.

51. Küng, A.; Pieper, T.; Wissiack, R.; Rosenberg, E.; Keppler, B. K. Hydrolysis of the tumor.inhibiting ruthenium(III) complexes Him *trans*-$[RuCl_4(im)_2]$ and Hind *trans*-$[RuCl_4(ind)_2]$ investigated by means of HPCE and HPLC-MS. *J. Biol. Inorg. Chem.* **2001**, *6*, 292–299.

52. Martin, R. B. In *Cisplatin: Chemistry and Biochemistry of a Leading Anticancer Drug*; Lippert, B., Ed.; VHCA & Wiley-VCH: Zürich, Switzerland, **1999**; pp. 181–205.

53. (a) Chanda, N.; Paul, D.; Kar, S.; Mobin, S. M:, Datta, A.; Puranik, V. G.; Rao, K. K.; Lahiri, G. K. Effect of 2-(2-pyridyl)azole-based ancillary ligands ($L^{1–4}$) on the electrophilicity of the nitrosyl function in $[Ru^{II}(trpy)(L^{1–4})(NO)]^{3+}$ [trpy = 2,2‘:6‘,2‘‘-terpyridine]. Synthesis, structures, and spectroscopic, electrochemical, and kinetic aspects. *Inorg. Chem.* **2005**, *44*, 3499–3511; (b) De, P.; Sarkar, B.; Maji, S.; Das, A. K.; Bulak, E.; Mobin, S. M.; Kaim, W.; Lahiri, G. K. Stabilization of $\{RuNO\}^6$ and $\{RuNO\}^7$ states in $[Ru^{II}(trpy)(bik)(NO)]^{n+}$ {trpy = 2,2′:6′,2′′-terpyridine, bik = 2,2′-bis(1-methylimidazolyl)ketone} – formation, reactivity, and photorelease of metal-bound nitrosyl. *Eur. J. Inorg. Chem*. **2009**, *2009*, 2702–2710; (c) De, P.; Mondal, T. K.; Mobin, S. M.; Sarkar, B.; Lahiri, G. K. $\{Ru–NO\}^6$ and $\{Ru–NO\}^7$ configurations in $[Ru(trpy)(tmp)(NO)]^{n+}$ (trpy = 2,2′:6′,2′′-terpyridine, tmp = 3,4,7,8-tetramethyl-1,10-phenanthroline): an experimental and theoretical investigation. *Inorg. Chim. Acta* **2010**, *363*, 2945–2954.

54. Enemark, J. H.; Feltham, R. D. Principles of structure, bonding and reactivity for metal nitrosyl complexes. *Coord. Chem. Rev.* **1974**, *13*, 339–406.
55. Rose, M. J.; Mascharak, P. K. Photoactive ruthenium nitrosyls: effects of light and potential application as NO donors. *Coord. Chem. Rev.* **2008**, *252*, 2093–2114.
56. P. Singh, B. Sarkar, M. Sieger, M. Niemeyer, J. Fiedler, S. Zalis, W. Kaim, The metal-NO interaction in the redox systems $[Cl_5Os(NO)]^{2+/+}$: calculations, structural, electrochemical, and spectroscopic results. *Inorg. Chem.* **2006**, *45*, 4602–4609.
57. Dyall, K. G. Relativistik double-zeta, triple-zeta, and quadruple-zeta basis sets for the 5d elements Hf–Hg. *Theor. Chem. Acc.* **2004**, *112*, 403–409.
58 Zink, J. R.; Abucayon, E. G.; Ramuglia, A. R.; Fadamin, A.; Eilers, J. E.; Richter-Addo, G. B.; Shaw, M. J. Electrochemical investigation of the kinetics of chloride substitution upon reduction of [Ru(porphyrin)(NO)Cl] complexes in tetrahydrofuran. *ChemElectroChem* **2017**, 4, 1–12.
59. Kaim, W. Complete and partial electron transfer involving coordinated NO^x. *Adv. Inorg. Chem.*, **2015**, 295–313.
60. Singh, P.; Das, A. K.; Sarkar, B.; Niemeyer, M.; Roncaroli, F.; Olabe, J. A.; Fiedler, J.; Záliš, S.; Kaim, W. Redox properties of ruthenium nitrosyl porphyrin complexes with different axial ligation: structural, spectroelectrochemical (IR, UV-visible and EPR), and theoretical studies. *Inorg. Chem.* **2008**, *47*, 7106–7113.
61. (a) L. J. Ignarro, Nitric Oxide: Biology and Pathobiology, Academic Press, San Diego, 2000; (b) M. Feelisch, J. S. Stamler, Nitric Oxide Research, John Wiley and Sons, Chichester, UK, 1996.
62. (a) Sieger, M.; Sarkar, B.; Zalis, S.; Fiedler, J.; Escola, N.; Doctorovich, F.; Olabe, J. A.; Kaim, W. Establishing the NO oxidation state in complexes $[Cl_5(NO)M]^{n-}$, M = Ru or Ir, through experiments and DFT calculations. *Dalton Trans.* **2004**, 1797–1800; (b) McCleverty, J. A. Reactions of nitric oxide coordinated to transition metals. *Chem. Rev.* **1979**, *79*, 53–76; (c) Wanner, M.; Scheiring, T.; Kaim, W.; Slep, L. D.; Baraldo, L. M.; Olabe, J. A.; Zalis, S.; Baerends, E. J. EPR characteristics of the $[(NC)_5M(NO)]^{3-}$ ions (M = Fe, Ru, Os). Experimental and DFT study establishing $NO^{\cdot}$ as a ligand. *Inorg. Chem.* **2001**, *40*, 5704–5707; (d) Haymore, B. L.; Ibers, J. A. Comparison of linear nitrosyl and singly bent aryldiazo complexes of ruthenium. Structures of trichloronitrosylbis(triphenylphosphine)-ruthenium, $RuCl_3(NO)(P(C_6H_5)_3)_2$, and trichloro(p-tolyl)diazobis(triphenylphosphine)-

ruthenium-dichloromethane, $RuCl_3(p\text{-}NNC_6H_4CH_3)(P(C_6H_5)_3)_2 \cdot CH_2Cl_2$. *Inorg. Chem.* **1975**, *14,* 3060–3070; (e) Gaughan, A. P.; Haymore, B. L.; Ibers, J. A.; Myers, W. H.; Nappier, T. F.; Meek, D. W. Extension of the nitrosyl-aryldiazo analogy. Structure of an aryldiazo group coordinated to rhodium and a doubly bent fashion. *J. Am. Chem. Soc.* **1973**, *95*, 6859–6861; (f) Pandey, K. K. Mononuclear d^7 complexes of platinum metals. *Coord. Chem. Rev.* **1992**, *121*, 1–42.

63. Snellenburg, J. J.; Laptenok, S. P.; Seger, R.; Mullen, K. M.; van Stokkum, I. H. M. Glotaran: A Java-based graphical user interface for the R package TIMP. *J. Stat. Softw.* **2012**, *49*, 1–22.

64. (a) Damrauer, N. H.; Cerullo, G.; Yeh, A.; Boussie, T. R.; Shank, C. V.; McCusker, J. K. Femtosecond dynamics of excited-state evolution in $[Ru(bpy)_3]^{2+}$. *Science* **1997**, *275*, 54–57; (b) Demas, J. N.; Adamson, A. W. A new photosensitizer. Tris(2,2′-bipyridine)ruthenium(II) chloride. *J. Amer. Chem. Soc.* **1971**, *93*, 1800–1801.

65. (a) Sun, Q.; Mosquera-Vasquez, S.; Daku, L. M. L.; Guénée, L.; Goodwin, H. A.; Vauthey, E.; Hauser, A. Experimental evidence of ultrafast quenching of the ^{3}MLCT luminescence in ruthenium(II) tris-bipyridyl complexes via a ^{3}dd state. *J. Amer. Chem. Soc.* **2013**, *135*, 13660–13663; (b) Imanbaew, D.; Nosenko, Y.; Kerner, C.; Chevalier, K.; Rupp, F.; Riehn, C.; Thiel, W. R.; Diller, R. Excited-state dynamics of a ruthenium(II) catalyst studied by transient photofragmentation in gas phase and transient absorption in solution. *Chem. Phys.* **2014**, *442*, 53–61.

66. Wallin, S.; Davidsson, J.; Modin, J.; Hammarström, L. Femtosecond transient absorption anisotropy study on $[Ru(bpy)_3]^{2+}$ and $[Ru(bpy)(py)_4]^{2+}$. Ultrafast interligand randomization of the MLCT state. *J. Phys. Chem A* **2005**, *109*, 4697–4704.

67. Freitag, L.; Gonzalez, L. Theoretical spectroscopy and photodynamics of a ruthenium nitrosyl complex. *Inorg. Chem*. **2014**, *53*, 6415–6426.

68. (a) Joseph, J.; Kalyanaraman, K.; Hyde, J. S. Trapping of nitric oxide ny nitronyl nitroxides: an electron spin resonance investigation. *Biochem. Biophys. Res. Commun.* **1993**, *192*, 926–936; (b) Silva Sousa, E. H.; Ridnour, L. A.; Gouveia, F. S.; Silva da Silva, C. D.; Wink, D. A.; de Franca Lopes, L. G.; Sadler, P. J. Thiol-Activated HNO Release from a Ruthenium Antiangiogenesis Complex and HIF-1α Inhibition for Cancer Therapy. *ACS Chem. Biol.* **2016**, 11, 2057–2065; (c) Bobko, A. A.; Bagryanskaya, E. G.; Reznikov, V. A.; Kolosova, N. G.; Clanton, T. L.; Khramtsov, V. V. Redox-sensitive mechanism of NO

scavenging by nitronyl nitroxides. *Free Radical Biol. Med.* **2004,** 36, 248–258; (d) Akaike, T.; Yoshida, M.; Miyamoto, Y.; Sato, K.; Kohno, M.; Sasamoto, K.; Miyazaki, K.; Ueda, S.; Maeda, H. Antagonistic action of imidazolineoxyl N-oxides against endothelium-derived relaxing factor/.bul.NO (nitric oxide) through a radical reaction. *Biochemistry* **1993**, 32, 827–832.

69. Cormary, D.; Malfant, I.; Buron-Le Cointe, M.; Toupet, L.; Delley, B.; Schaniel, D.; Mockus, N.; Woike, T.; Fejfarová, K.; Petrícek, V.; Dusek, M. $[Ru(py)_4Cl(NO)][PF_6]_2 \cdot 0.5H_2O$: a model system for structural determination and *ab initio* calculations of photo-induced linkage NO isomers. *Acta Cryst.* **2009**, *B65*, 612–623.

70. Cormary, B.; Ladeira, S.; Jacob, K.; Lacroix, P. G.; Woike, T.; Schaniel, D.; Malfant, I. Structural influence of the photochromic response of a series of ruthenium mononitrosyl complexes. *Inorg. Chem.* **2012**, *51*, 7492–7501.

71. (a) Radoń, M.; Pierloot, K. Binding of CO, NO, and O_2 to Heme by Density Functional and Multireference ab Initio Calculations. *J. Phys. Chem. A* **2008**, *112*, 11824–11832; (b) Radoń, M.; Broclawik, E.; Pierloot, K. Electronic Structure of Selected $\{FeNO\}^7$ Complexes in Heme and Non-Heme Architectures: A Density Functional and Multireference ab Initio Study. *J. Phys. Chem. B* **2010**, *114*, 1518–1528; (c) De, P.; Maji, S.; Chowdhury, A. D.; Mobin, S. M.; Mondal, T. K.; Paretzki, A.; Lahiri, G. K. Ruthenium nitrosyl complexes with 1,4,7-trithiacyclononane and 2,2′-bipyridine (bpy) or 2-phenylazopyridine (pap) coligands. Electronic structure and reactivity aspects. *Dalton Trans*. **2011**, *40*, 12527–12539.

72. Trondl, R.; Heffeter, P.; Kowol, C. R.; Jakupec, M. A.; Berger, W.; Keppler, B. K. NKP-1339, the first ruthenium-based anticancer drug on the edge to clinical application. *Chem. Sci.* **2014,** 5, 2925–2932.

73. Henke, M. M.; Richly, H.; Drescher, A.; Grubert, M.; Alex, D.; Thyssen, D.; Jaehde, U.; Scheulen, M. E.; Hilger, R. A. Pharmacokinetic study of sodium trans-[tetrachlorobis(1H-indazole)-ruthenate (III)]/-indazole hydrochloride (1:1:1) (FFC14A) in patients with solid tumors. *Int. J. Clin. Pharmacol. Ther.* **2009,** 47, 58–60.

74. Lentz, F.; Drescher, A.; Lindauer, A.; Henke, M.; Hilger, R. A.; Hartinger, C. G.; Scheulen, M. E.; Dittrich, C.; Keppler, B. K.; Jaehde, U. Pharmacokinetics of a novel anticancer ruthenium complex (KP1019, FFC14A) in a phase I dose-escalation study. *Anti-Cancer Drugs* **2009**, 20, 97–103.

75. Maeda, H.; Akaike, T.; Yoshida, M.; Suga, M. Multiple functions of nitric oxide in pathophysiology and microbiology: analysis by a new nitric oxide scavenger. *J. Leukocyte Biol.* **1994,** 56, 588–592.

76. Sanchez, d. M. L.; Casado, S.; Farre, J.; Garcia-Duran, M.; Rico, L. A.; Monton, M.; Romero, J.; Bellver, T.; Sierra, M. P.; Guerra, J. I.; Mata, P.; Esteban, A.; Lopez-Farre, A. Comparison of in vitro effects of triflusal and acetysalicylic acid on nitric oxide synthesis by human neutrophils. *Eur J Pharmacol* **1998**, 343, 57–65.

77. Maeda, H.; Akaike, T.; Yoshida, M.; Suga, M. Multiple functions of nitric oxide in pathophysiology and microbiology: analysis by a new nitric oxide scavenger. *J. Leukocyte Biol.* **1994,** 56, 588–592.

78. Zamora, R.; Bult, H.; Herman, A. G. The role of prostaglandin E2 and nitric oxide in cell death in J774 murine macrophages. *Eur. J. Pharmacol.* **1998,** 349, 307–315.

79. Gurpinar, E.; Vousden, K. H. Hitting cancers' weak spots: vulnerabilities imposed by p53 mutation. *Trends Cell Biol.* **2015**, 25, 486–495.

80. Muller, P. A. J.; Vousden, K. H. Mutant p53 in Cancer: New Functions and Therapeutic Opportunities. *Cancer Cell* **2014**, 25, 304–317.

81. Gudkov, A. V.; Komarova, E. A. Prospective therapeutic applications of p53 inhibitors. *Biochem. Biophys. Res. Commun.* **2005**, 331, 726–736.

82. Sohn, D.; Graupner, V.; Neise, D.; Essmann, F.; Schulze-Osthoff, K.; Jaenicke, R. U. Pifithrin-α protects against DNA damage-induced apoptosis downstream of mitochondria independent of p53. *Cell Death Differ.* **2009**, 16, 869–878.

83. Heffeter, P.; Pongratz, M.; Steiner, E.; Chiba, P.; Jakupec, M. A.; Elbling, L.; Marian, B.; Koerner, W.; Sevelda, F.; Micksche, M.; Keppler, B. K.; Berger, W. Intrinsic and acquired forms of resistance against the anticancer ruthenium compound KP1019 indazolium trans-[tetrachlorobis(1*H*-indazole)ruthenate (III)] (FFC14A). *J. Pharmacol. Exp. Ther.* **2005**, 312, 281–289.

84. Chow, M. J.; Babak, M. V.; Wong, D. Y. Q.; Pastorin, G.; Gaiddon, C.; Ang, W. H. Structural Determinants of p53-Independence in Anticancer Ruthenium-Arene Schiff-Base Complexes. *Mol. Pharm.* **2016**, 13, 2543–2554.

85. Abbas, T.; Dutta, A. p21 in cancer: intricate networks and multiple activities. *Nat. Rev. Cancer* **2009**, 9, 400–414.

Table of Contents

(Graphical Abstract)

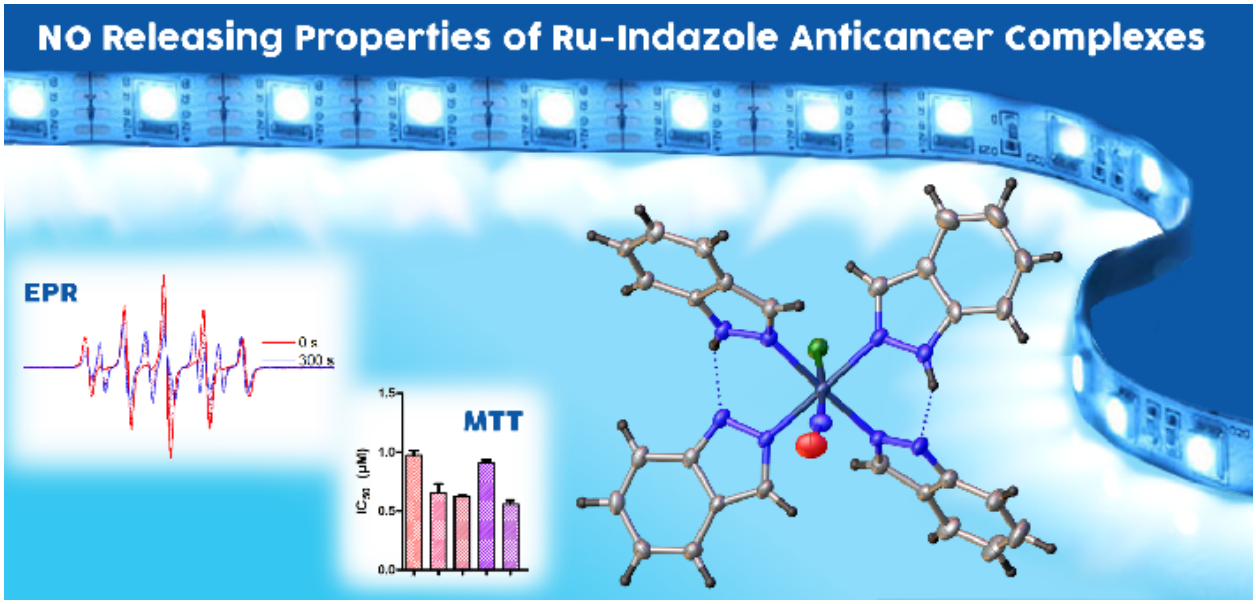

Our findings suggest that ruthenium-nitrosyl complexes with equatorial 1*H*-indazole ligands and chlorido or hydroxido ligand in trans-position to NO^+ are very effective antiproliferative agents. The indazole ligands in parent complexes undergo deprotonation at physiological pH with formation of electroneutral inner sphere complexes. The photo-induced release of NO upon irradiation has been confirmed both in the solid state by IR spectroscopy and in solution by EPR spectroscopy.